Received: Added at production | Revised: Added at production | Accepted: Added at production

DOI: xxx/xxxx

ARTICLE TYPE

An Incremental-Secant Mean-Field Homogenization Model Enhanced With a Non-Associated Pressure-Dependent Plasticity Model

Juan Manuel Calleja Vázquez[1,2] | Ling Wu[1] | Van-Dung Nguyen[1] | Ludovic Noels*[1]

[1]Computational & Multiscale Mechanics of Materials, Liege Universite, Liège, Belgium
[2]F.R.S.-FNRS, Rue d'Egmont 5 - B 1000 Bruxelles

Correspondence
*Liege Universite, CM3 B52, Allée de la découverte 9, B4000 Liège, Belgium. Email: jmcalleja@uliege.be, l.wu@ulg.ac.be, vandung.nguyen@uliege.be, l.noels@ulg.ac.be

Summary

This paper introduces a, possibly damage-enhanced, pressure-dependent based incremental-secant mean-field homogenization (MFH) scheme for two-phase composites. The incremental-secant formulation consists on a fictitious unloading of the material up to a stress-free state, in which a residual stress is attained in its phases. Then the secant method is performed in order to compute the mean stress fields of each phase. One of the main advantages of this method is the natural isotropicity of the secant tensors that allows defining the Linear-Comparison-Composite (LCC). In this work, we show that this isotropic nature is preserved for a non-associated pressure dependent plastic flow, making possible the direct definition of the LCC. This model is thus able to represent the physics of real polymeric composites. The MFH scheme is then verified by testing its prediction capabilities in several cases, including cyclic and non-proportional loading involving perfectly elastic phases, elasto-plastic and damage-enhanced elasto-plastic phases in random Representative Volume Elements (RVE) of Uni-Directional (UD) composites and of composites reinforced with spherical inclusions.

KEYWORDS:
Mean-Field Homogenization, Incremental-Secant, Pressure-Dependent Yield, Damage, Non-local

1 | INTRODUCTION

The use of composite materials has introduced new challenges within the industry, as the complex microstructure makes the use of direct numerical simulations unfeasible due to the high computational cost. In order to avoid this computing bottleneck, several homogenization techniques have been developed as shown by many reviews such as Kanouté et al.[1], Geers et al.[2], Llorca et al.[3], Nemat-Nasser and Hori[4] and Noels et al.[5]. These techniques allow retaining the constituents behavior into consideration when performing composite simulations while avoiding the need for resolving all the details of the complex microstructure behavior.

Some examples of homogenization techniques are Ghosh et al.[6] Voronoi cell finite element method (VCFEM), a purely numerical method which combines the asymptotic homogenization technique with the microstructural modeling using Voronoi cells, Lissenden and Arnold's method of cells[7], the unit cell finite element (FE)-based computations (Wieckowski[8]; Segurado et al.[9] ; Ji and Wang[10]; Carrere et al.[11]), the generalizations of the VCFEM method by Michel et al.[12], Feyel[13], Terada et al.[14] or Kouznetsova[15] in which a finite element model of the RVE was associated to each macro-scale integration point that led to the FE2 method ([15],[16]), or the mean-field homogenization (MFH) method, which is considered in this paper.

The main goal of Mean-Field Homogenization is to avoid the computation of the detailed micro-strain or stress fields by assuming relations between the volume averages of the strain and stress fields of each material phase. Some of the advantages that MFH presents over other homogenization techniques are its easiness of implementation in a FE code as a material law, its semi-analytical nature and low computational requirements.

The fundamental solution derived by J.D. Eshelby for single ellipsoidal inclusions [17] served as a basis for the first Mean-Field Homogenization (MFH) methods for linear-elastic cases and it is still considered as one of the most important solutions used in MFH. Most of the current models are still based on this fundamental solution, among which we can find the self-consistent model ([18],[19],[20]) which is mostly applicable for high inclusion volume fractions or poly-crystalline materials, the incremental or differential models [21], or the Mori-Tanaka (M-T) model [22]. By using similar steps to the ones used by Eshelby [17] on its single inclusion solution and applying it to a multiple-inclusions RVE, the M-T model is one of the most widely used MFH models for low and moderate inclusion volume fractions due to its ease of use and accurate predictions for 2-phase composite materials. However, not all MFH methods are directly based on the Eshelby solution, as it is the case of the composite sphere assemblage proposed by Hashin [23], the generalized self-consistent (GSC) by Christensen and Lo [24], which was based on the composite sphere assemblage and the double inclusion model (Nemat-Nasser and Hori [25]), that took inspiration from the GSC model formulating the ellipsoidal inclusions similarly to the M-T model.

Even though MFH models were initially developed for linear behaviors, they can be extended in order to represent material nonlinearities with very low computational cost. The most common approach is the definition of a Linear Comparison Composite (LCC). An LCC is a fictitious material defined from linear phases with the same behavior as the linearized behavior of the studied material. The LCC can be defined through different approaches, as for example through direct linearization of the nonlinear constitutive models of the material phases or through variational formulations. The single potential approach pioneered by Ponte Castañeda ([26],[27]), the two-potential approach by Lahellec and Suquet ([28],[29]) or the incremental variational ([30],[31],[32],[33],[34],[35]) formulations are some examples of variational formulations. The direct linearization approach for the definition of the LCC is used in the secant formulation by Berveiller and Zaoui [36]; Tandon and Weng [37]; etc., a formulation which allows representing visco-plastic behaviors under proportional and monotonic loading conditions. Other approaches are the affine formulation ([38],[39],[40], etc.) which is valid for arbitrary loading history of visco-plastic models, the incrementally affine formulation ([41];[42]), or the incremental-tangent formulation ([19],[43],[44],[45] etc.), which allows representing arbitrary loading. There is one main drawback when using the affine, incrementally-affine and incremental-tangent formulations, which is the anisotropicity of their tangent operators. This generally leads to a stiff behavior, yielding inaccurate MFH predictions. In order to improve the MFH solution, it is possible to isotropize the tangent operators when computing the strain concentration tensors [46]. This step is not needed in the case of the incremental-secant linearization ([47],[48],[49],[50]) since its material operators are isotropic by nature. The incremental-secant linearization first applies a fictitious elastic unloading to the studied composite material at a given step configuration. While the composite material reaches a zero stress state, this is not the case for each of the phases, as these can have a residual stress. Then, the composite is re-loaded until reaching the new composite configuration in the next step. The secant operators of each phase, which are naturally isotropic, are then used to define the LCC. This formulation allows for good accuracy in non-proportional loading conditions and damage-enhanced elasto-plastic cases [48].

Even though nowadays multiscale homogenization methods are capable of representing accurately the non-linear behavior of composite materials as shown by Pierard et al. [51], the representation of fracture or damage can introduce some difficulties, as a loss of ellipticity is found in the governing equations of the MFH formulation at the strain-softening onset ([3],[2]). This loss of ellipticity causes the finite element solution to be non-unique, introducing a high mesh dependence. In order to address this issue, higher order terms could be introduced into the governing equations as presented in the overview by De Borst et al. [52], making possible an interaction between a given point and its surroundings through the introduction of a characteristic length associated with the failure mechanisms and micro-structure of the studied material. Some examples of formulations that address this strain-softening problem are the non-local averaging approach developed by Bažant [53], the gradient-dependent flow theory by Zbib and Aifantis [54], or the reappraisal of the Cosserat continuum model by De Borst [55]. Even though these formulations could circumvent the non-unique solution problem, these higher order terms introduce also the need to solve higher-order derivatives, increasing the complexity of these models. By formulating the non-local approach implicitly, a new non-local variable emanates as a result of the resolution of a new boundary value problem. This was proposed in the context of homogeneous materials by Peerlings et al. [56]; Geers [57]; Peerlings et al. [58] and it is based on a weighted averaging integral in a new partial differential equation, making the formulation fully non-local. This is not the case in other non-local formulations based on the introduction of higher-order terms as in the works by Aifantis [59], or by Svedberg and Runesson [60].

These non-local and higher-order formulations are more commonly used in direct numerical simulations than in multiscale simulations. However, in 1999, Knockaert and Doghri[61] implemented a nonlocal constitutive model with gradients of internal variables for the one dimensional case, the Cosserat model was applied in the Mori-Tanaka model by Liu and Hu[62] and Coenen et al.[63 64] who generalized the Massart et al.[65 66] non-local approach for masonry wall computations, showing the possibility to apply this approach to semi-analytical or numerical computational homogenizations. In 2013, Wu et al.[47] implemented an implicit-gradient-enhanced approach of the incremental-secant MFH scheme, which permitted to account for damage in UD composite simulations while retaining the main benefits of the incremental-secant formulation.

The incremental-secant approach was developed by Wu et al. ([47],[67]) by considering J2 plasticity in the different phases, meaning this approach was only valid for pressure insensitive materials. However, to be representative of the behavior of polymer based materials, the phases response should account for a pressure dependent behavior. Such is the case for amorphous glassy polymers, which can present a high pressure dependence. This behavior was studied and modeled on fully discretized microstructures by Nguyen et al. ([68],[69]), who implemented a hyperelastic viscoelastic-viscoplastic-damage constitutive model based on a multi-mechanism non-local damage continuum to model the matrix phase of the composite material. This model showed great capabilities to mimic real epoxy materials like the high-crosslinked RTM6 epoxy resin[69]. However, the resolution time of this full discretization remains prohibitive, motivating the development of MFH embedding pressure-dependent phases. The behavior of polymeric material can be captured by considering a yield surface written in terms of the pressure and equivalent stress in combination with a non-associated plastic potential flow depending on the same two parameters defining the volume variation during plastic flow ([68,69,70,71]). In this work, it is thus intended to model the matrix phase of the composite material with the power-enhanced version of the pressure dependent yield surface in combination with the non associated plastic potential developed by Nguyen et al.[68]. The anisotropic and more complex behavior of the composite material naturally arises from the homogenization process.

Pressure-sensitive models have been applied in homogenization methods, especially in homogenization of rock-like and porous materials, where taking into consideration the hydrostatic pressure effect on the material behavior is of crucial importance. Such is the case of Abou-Chakra Guéry et al.[72], who developed a two-step homogenization procedure to study the behavior of Callovo-Oxfordian argillites or Shen et al.[73] who studied the mechanical behavior of clayey rocks with a plastic compressible porous matrix. Both works based their non-linear homogenization techniques on an adaptation of the incremental method proposed by Hill[19], which formulates the macroscopic tangent operator accounting for nonlinear local behaviors on each phase of the composite. One of the main drawbacks of this procedure is the stiff behavior that the homogenized results present at the macroscopic level. In order to solve this problem, both works opted to implement an isotropization technique to improve the obtained material response. In order to capture the pressure sensitive behavior of these materials, the Drucker-Prager-based yield criteria was used in both works. Composite materials are also a domain in which the hydrostatic pressure effects are important. An example is the work by Kaiser et al.[74], which focused on improving the modeling of short fiber reinforced thermoplastics by using the quadratic yield formulation proposed by Kolling et al.[75]. This yield criterion was implemented in the second moment incremental formulation based MFH approach developed for elastic-plastic composites by Doghri et al.[76]. As for the previous cases, an isotropization step was needed in order to avoid over-stiff behaviors, for which the isotropization proposed by Bornert[77] was applied. Other approaches such as introducing a pressure sensitivity in the damage evolution law have been studied, although, wrong predictions were obtained. Such is the case of A. Krairi[78], who proved that the introduction of pressure-sensitivity in the damage law evolution was not enough to capture the correct pressure effect on the studied materials.

The aim of this work is to consider a pressure-dependent yield criterion based on Nguyen et al.'[68] constitutive model in Wu et al.' ([67],[47]) incremental-secant approach. We will show that the incremental-secant approach allows defining naturally isotropic operators for pressure-sensitive models, circumventing the need for an isotropization step as in other formulations. We will also show that the approach inherits the benefits of the incremental-secant approach, i.e. its ability to consider damaging phases and to remain accurate under non-proportional loading conditions. The implementation enables thus to take into account this pressure-dependent behavior observed in polymer-based materials while keeping the mentioned .

Regarding the structure of this paper, Section 2 starts by presenting a recall of MFH incremental-secant generalities.
When considering homogenization of composite materials through a MFH scheme, scalar damage variables can be considered in each phase in order to capture the composite response[79]. In this work, we consider the damage of the matrix phase only since we are interested in accounting for the effect of the pressure-dependent yield surface on the homogenization scheme. In that case, it was shown by Nguyen et al.[68] that a scalar damage variable framed in a Lemaitre-Chaboche damage model was able to capture the failure of highly cross-linked polymer materials, including in 3D tests with barreling effects. In their work[68], the authors also considered a second damage variable to capture the post-peak saturated softening observed under compressive loading,

which is neglected in the present paper: introducing this second scalar damage variable in the model does not require to modify the formulation since an equivalent damage variable can be obtained from two damage evolution laws. Then, Section 3 opens with a brief introduction of the pressure-sensitive yield function used and continues with its mathematical implementation in the residual incremental-secant approach. Section 4 introduces then the pressure-sensitive mean-field homogenization scheme. This MFH scheme is later verified in Section 5 for the elasto-plastic and damage-enhanced elasto-plastic cases by comparing the MFH predictions to full-field FE simulations on 2D UD composite RVE and 3D composites reinforced with spherical inclusions. In Section 6, the approach is further validated against a macro-scale transverse compression experiment performed on a UD composite sample.

2 | MFH RECALL

In this section, a brief presentation of the basis of the MFH method using the Mori-Tanaka assumption is provided. Then, the incremental-secant MFH is recalled introducing the residual and zero incremental-secant operators.

2.1 | MFH generalities

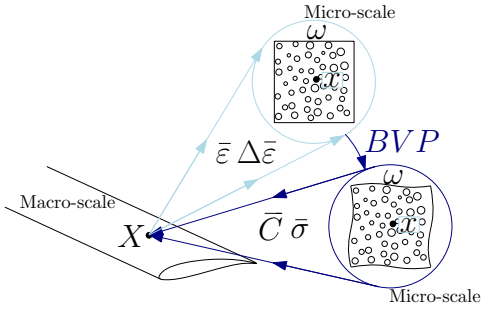

FIGURE 1 Multi-scale simulation scheme.

Considering a multiscale problem (Fig. 1), two different scales are present: the macro-scale and the micro-scale. At the macro-scale, either the macro-strain $\bar{\boldsymbol{\varepsilon}}$ or the macro-stress $\bar{\boldsymbol{\sigma}}$ is known at a given point $\boldsymbol{X}$ and the unknown quantity is obtained by solving a micro-scale boundary-value problem (BVP). This point $\boldsymbol{X}$, from a micro-scale perspective, represents a set of points $\boldsymbol{x}$ that belongs to an RVE domain such that $\mathbf{x} \in \omega$ with a boundary $\partial\omega$. As a two-phase composite material is taken into account, the sub-index 0 represents the matrix subdomain (ω_0) and the sub-index I the inclusion subdomain (ω_I).

As already stated, MFH assumes relations between volume averages of the stress or strain fields of each phase, which avoids the high computational requirements needed for the complete resolution of the micro-strain / stress fields. The scale transition is written as a relation between the macro-strains and stresses and the RVE average strains $\langle\boldsymbol{\varepsilon}\rangle_\omega$ and stresses $\langle\boldsymbol{\sigma}\rangle_\omega$ with the following relation: $\langle f(\boldsymbol{x})\rangle_\omega = \frac{1}{V_\omega}\int_\omega f(\boldsymbol{x})\mathrm{d}V$. Therefore, the relation between the macro-strain and stress and the averaged RVE quantities can be written as follows:

$$\begin{aligned}\bar{\boldsymbol{\varepsilon}} &= \langle\boldsymbol{\varepsilon}\rangle_\omega = v_0\langle\boldsymbol{\varepsilon}\rangle_{\omega_0} + v_\mathrm{I}\langle\boldsymbol{\varepsilon}\rangle_{\omega_\mathrm{I}},\\ \bar{\boldsymbol{\sigma}} &= \langle\boldsymbol{\sigma}\rangle_\omega = v_0\langle\boldsymbol{\sigma}\rangle_{\omega_0} + v_\mathrm{I}\langle\boldsymbol{\sigma}\rangle_{\omega_\mathrm{I}},\end{aligned} \tag{1}$$

where v_0 and v_I stand for the matrix and inclusions volume fractions respectively, having that $v_0 + v_\mathrm{I} = 1$. For notation simplicity, $\langle\bullet\rangle_{\omega_i}$ is replaced by $\bullet_i$ in the following equations.

In linear elasticity, the MFH model relates the strain fields of each phase by means of a strain-concentration tensor as:

$$\boldsymbol{\varepsilon}_\mathrm{I} = \boldsymbol{B}^\epsilon\left(\mathrm{I}, \boldsymbol{C}_0^{\mathrm{el}}, \boldsymbol{C}_\mathrm{I}^{\mathrm{el}}\right) : \boldsymbol{\varepsilon}_0, \tag{2}$$

where the strain concentration tensor $\boldsymbol{B}^\epsilon$ is defined from the phases elasticity operators $\boldsymbol{C}_0^{\mathrm{el}}$ and $\boldsymbol{C}_\mathrm{I}^{\mathrm{el}}$ using the Mori-Tanaka model[22] as:

$$\boldsymbol{B}^\epsilon = \left\{\boldsymbol{I} + \boldsymbol{S} : \left[\left(\boldsymbol{C}_0^{\mathrm{el}}\right)^{-1} : \boldsymbol{C}_\mathrm{I}^{\mathrm{el}} - \boldsymbol{I}\right]\right\}^{-1}, \tag{3}$$

where $\boldsymbol{I}$ is the fourth order identity tensor and where $\boldsymbol{S}\left(\mathrm{I}, \boldsymbol{C}_0^{\mathrm{el}}\right)$ is the Eshelby tensor[17] that depends on the geometry of the inclusions (I) and the matrix elastic operator $\boldsymbol{C}_0^{\mathrm{el}}$.

For non-linear behaviors, the virtual elastic operators $\boldsymbol{C}_0^{\mathrm{LCC}}$ and $\boldsymbol{C}_{\mathrm{I}}^{\mathrm{LCC}}$ of the matrix and the inclusions respectively define the LCC and allow formulating the relation between the averaged incremental strains of both composite phases thanks to the strain concentration tensor $\boldsymbol{B}^{\epsilon}$ as

$$\Delta\boldsymbol{\varepsilon}_{\mathrm{I}} = \boldsymbol{B}^{\epsilon}\left(\mathrm{I}, \boldsymbol{C}_0^{\mathrm{LCC}}, \boldsymbol{C}_{\mathrm{I}}^{\mathrm{LCC}}\right) : \Delta\boldsymbol{\varepsilon}_0. \tag{4}$$

By using the virtual elastic operators $\boldsymbol{C}_0^{\mathrm{LCC}}$ and $\boldsymbol{C}_{\mathrm{I}}^{\mathrm{LCC}}$ of the LCC, the Mori-Tanaka model[22] that defines $\boldsymbol{B}^{\epsilon}$ is rewritten as:

$$\boldsymbol{B}^{\epsilon} = \left\{\boldsymbol{I} + \boldsymbol{S} : \left[\left(\boldsymbol{C}_0^{\mathrm{LCC}}\right)^{-1} : \boldsymbol{C}_{\mathrm{I}}^{\mathrm{LCC}} - \boldsymbol{I}\right]\right\}^{-1}. \tag{5}$$

2.2 | Incremental-secant MFH

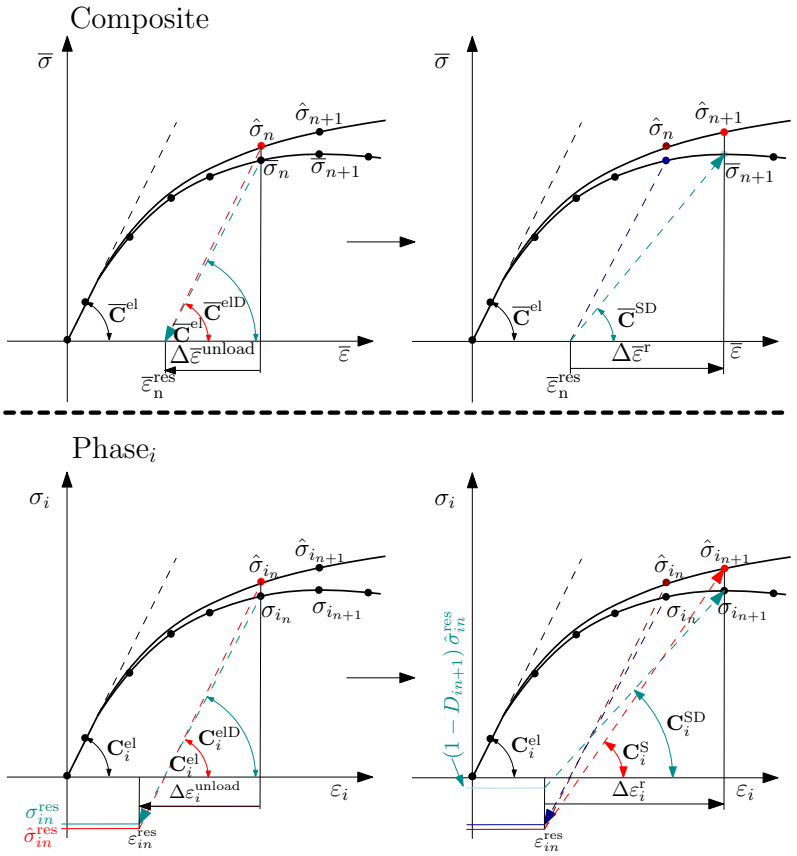

FIGURE 2 Representation of the damage-enhanced incremental-secant formulation for the composite material and for a composite material phase.

Let us consider a time step interval $[t_n, t_{n+1}]$ in which strain increments $\Delta\bar{\boldsymbol{\varepsilon}}_{n+1}$ and $\Delta\boldsymbol{\varepsilon}_{i_{n+1}}$ are applied to the composite material and its phases respectively, such that the total strain at t_{n+1} yields:

$$\bar{\boldsymbol{\varepsilon}}_{n+1} = \bar{\boldsymbol{\varepsilon}}_n + \Delta\bar{\boldsymbol{\varepsilon}}_{n+1} \text{ and } \boldsymbol{\varepsilon}_{i_{n+1}} = \boldsymbol{\varepsilon}_{i_n} + \Delta\boldsymbol{\varepsilon}_{i_{n+1}}. \tag{6}$$

For the sake of generality, a damage enhanced case formulated following a Lemaitre-Chaboche approach is considered. In this case, the elasto-plastic (EP) flow is evaluated in the apparent stress state $\left(\hat{\boldsymbol{\sigma}}_i = \frac{\boldsymbol{\sigma}_i}{(1-D_i)}\right)$, where D_i is the phase damage variable, and we thus consider in the following the latter case.

2.2.1 | Virtual elastic unloading

As recalled in the introduction, the incremental-secant approach first virtually unloads the composite material to a zero-stress state (see Fig. 2), but this is not necessarily the case for the phases composing the composite material, since each sees a residual stress $\hat{\boldsymbol{\sigma}}_{i_n}^{\text{res}}$. One thus defines the unloading and residual stress states as:

$$\begin{aligned} \bar{\boldsymbol{\sigma}}_n^{\text{res}} &= 0 = \bar{\boldsymbol{\sigma}}_n - \bar{\boldsymbol{C}}^{\text{elD}} \Delta\bar{\boldsymbol{\varepsilon}}^{\text{unload}}, \\ \hat{\boldsymbol{\sigma}}_{i_n}^{\text{res}} &= \hat{\boldsymbol{\sigma}}_{i_n} - \boldsymbol{C}_i^{\text{elD}} \Delta\boldsymbol{\varepsilon}_i^{\text{unload}}, \end{aligned} \tag{7}$$

where $\Delta\boldsymbol{\varepsilon}_i^{\text{unload}} = \boldsymbol{\varepsilon}_{i_n} - \boldsymbol{\varepsilon}_{i_n}^{\text{res}}$, being $\boldsymbol{\varepsilon}_{i_n}^{\text{res}}$ the phase strain reached at this composite zero-stress state, $\Delta\bar{\boldsymbol{\varepsilon}}^{\text{unload}} = \bar{\boldsymbol{\varepsilon}}_n - \bar{\boldsymbol{\varepsilon}}_n^{\text{res}}$, where $\bar{\boldsymbol{\varepsilon}}_n^{\text{res}}$ is the composite strain when reaching the zero-stress state, $\bar{\boldsymbol{C}}^{\text{elD}}$ and $\boldsymbol{C}_i^{\text{elD}}$ are the macro-scale and phase damaged elastic operators which are respectively defined as:

$$\begin{aligned} &\bar{\boldsymbol{C}}^{\text{elD}}\left(\text{I}, \boldsymbol{C}_0^{\text{elD}}, \boldsymbol{C}_{\text{I}}^{\text{elD}}\right) = \left[v_{\text{I}}\boldsymbol{C}_{\text{I}}^{\text{elD}} : \boldsymbol{B}^{\epsilon}\left(\text{I}, \boldsymbol{C}_0^{\text{elD}}, \boldsymbol{C}_{\text{I}}^{\text{el}}\right) + v_0\boldsymbol{C}_0^{\text{elD}}\right] : \left[v_{\text{I}}\boldsymbol{B}^{\epsilon}\left(\text{I}, \boldsymbol{C}_0^{\text{elD}}, \boldsymbol{C}_{\text{I}}^{\text{elD}}\right) + v_0\boldsymbol{I}\right]^{-1}, \text{ and} \\ &\boldsymbol{C}_i^{\text{elD}} = (1 - \boldsymbol{D}_{i_n})\boldsymbol{C}_i^{\text{el}}. \end{aligned} \tag{8}$$

Considering the residual strain tensors, Eq. (6) can be rewritten as:

$$\begin{aligned} \bar{\boldsymbol{\varepsilon}}_{n+1} &= \bar{\boldsymbol{\varepsilon}}_n^{\text{res}} + \Delta\bar{\boldsymbol{\varepsilon}}_{n+1}^{\text{r}}, \\ \boldsymbol{\varepsilon}_{i_{n+1}} &= \boldsymbol{\varepsilon}_{i_n}^{\text{res}} + \Delta\boldsymbol{\varepsilon}_{i_{n+1}}^{\text{r}}, \end{aligned} \tag{9}$$

where $\Delta\boldsymbol{\varepsilon}_{i_{n+1}}^{\text{r}}$ is the phase strain increment from the residual strain to the new strain $\boldsymbol{\varepsilon}_{n+1}$ and where $\Delta\bar{\boldsymbol{\varepsilon}}_{n+1}^{\text{r}}$ is the composite strain increment from the residual strain to the new strain $\bar{\boldsymbol{\varepsilon}}_{n+1}$ as shown graphically in Fig. 2. In this work, we consider the damage of the matrix phase only since we are interested in accounting for the effect of the pressure-dependent yield surface on the homogenization scheme. Assuming damage is only present in the matrix phase of the composite material from now on, it is possible to write the final system of equations as:

$$\begin{aligned} &\bar{\boldsymbol{\sigma}}_n - \bar{\boldsymbol{C}}^{\text{elD}}\left(\text{I}, \boldsymbol{C}_0^{\text{elD}}, \boldsymbol{C}_{\text{I}}^{\text{el}}\right) : \Delta\bar{\boldsymbol{\varepsilon}}^{\text{unload}} = 0, \\ &\Delta\bar{\boldsymbol{\varepsilon}}^{\text{unload}} = v_0\Delta\boldsymbol{\varepsilon}_0^{\text{unload}} + v_{\text{I}}\Delta\boldsymbol{\varepsilon}_{\text{I}}^{\text{unload}}, \\ &\Delta\boldsymbol{\varepsilon}_{\text{I}}^{\text{unload}} = \boldsymbol{B}^{\epsilon}(\text{I}, \boldsymbol{C}_0^{\text{elD}}, \boldsymbol{C}_{\text{I}}^{\text{el}}) : \Delta\boldsymbol{\varepsilon}_0^{\text{unload}}. \end{aligned} \tag{10}$$

2.2.2 | Incremental-secant loading

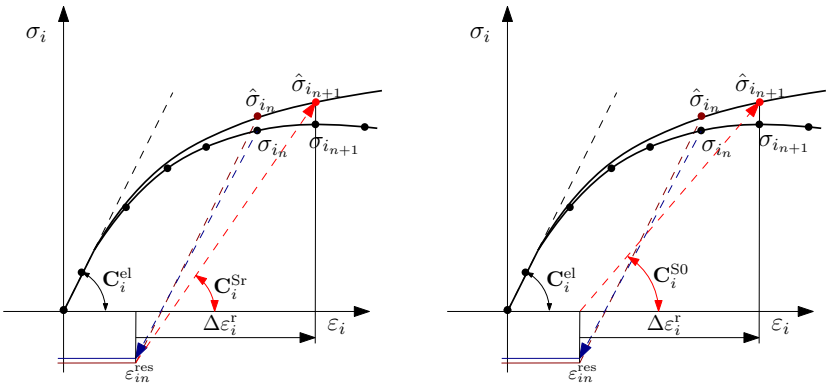

FIGURE 3 Graphical representation of the definition of the residual-secant operator (left) and the zero-secant operator (right).

The virtually unloaded composite material is then reloaded, until reaching the new stress-state. The computation of this reloading is made by defining a LCC subjected to a strain increment $\Delta\bar{\boldsymbol{\varepsilon}}_{n+1}^{\text{r}}$ from which the stress tensor is computed. The phases effective stress tensor at t_{n+1} can be defined from the stress increment such that:

$$\hat{\boldsymbol{\sigma}}_{i_{n+1}} = \hat{\boldsymbol{\sigma}}_{i_n}^{\text{res}} + \Delta\hat{\boldsymbol{\sigma}}_{i_{n+1}}^{\text{r}}, \tag{11}$$

being $\Delta\hat{\boldsymbol{\sigma}}^{\mathrm{r}}_{i_{n+1}}$ defined as:

$$\Delta\hat{\boldsymbol{\sigma}}^{\mathrm{r}}_{i_{n+1}} = \boldsymbol{C}^{\mathrm{Sr}}_{i} \,:\, \Delta\boldsymbol{\varepsilon}^{\mathrm{r}}_{i_{n+1}}, \tag{12}$$

where $\boldsymbol{C}^{\mathrm{Sr}}_{i}$ is the residual-incremental-secant operator of the elasto-plastic material. The computation of this residual-incremental-secant operator is detailed later in this paper, but its physical interpretation is illustrated in Fig. 3 (left).

As lengthily discussed by Wu et al. ([48],[47],[49]), when considering only first statistical moments, the incremental-secant method main limitation is the over-stiff results predicted when studying composites whose elasto-plastic inclusions are much stiffer than the matrix phase during the plastic flow. It was shown for a wide variety of test cases that by neglecting the residual stress in the matrix phase, see Fig. 3, this over-stiffness was counterbalanced. This is called the zero-incremental secant method. The need for this zero-incremental secant can be circumvented with the use of a second second statistical moments[49]. In the zero-incremental case, the new effective stress tensor would be defined by means of the zero secant operator $\boldsymbol{C}^{\mathrm{S0}}_{i}$ as:

$$\hat{\boldsymbol{\sigma}}^{\mathrm{r}}_{i_{n+1}} = \boldsymbol{C}^{\mathrm{S0}}_{i} \,:\, \Delta\boldsymbol{\varepsilon}^{\mathrm{r}}_{i_{n+1}}, \tag{13}$$

Using $\boldsymbol{C}^{\mathrm{S}}$, standing for either $\boldsymbol{C}^{\mathrm{Sr}}$ or $\boldsymbol{C}^{\mathrm{S0}}$, we can define the LCC using the strain concentration tensor:

$$\boldsymbol{B}^{\epsilon}\left(\mathrm{I}, \left(1 - D_{0_{n+1}}\right)\boldsymbol{C}^{\mathrm{S}}_{0}, \boldsymbol{C}^{\mathrm{S}}_{\mathrm{I}}\right), \tag{14}$$

being possible to close the system of equations that writes:

$$\begin{aligned}
&\Delta\bar{\boldsymbol{\varepsilon}}^{\mathrm{r}} = v_0\Delta\boldsymbol{\varepsilon}^{\mathrm{r}}_{0} + v_1\Delta\boldsymbol{\varepsilon}^{\mathrm{r}}_{\mathrm{I}},\\
&\Delta\boldsymbol{\varepsilon}^{\mathrm{r}}_{\mathrm{I}} = \boldsymbol{B}^{\epsilon}\left(\mathrm{I}, \boldsymbol{C}^{\mathrm{SD}}_{0}, \boldsymbol{C}^{\mathrm{S}}_{\mathrm{I}}\right) \,:\, \Delta\boldsymbol{\varepsilon}^{\mathrm{r}}_{0},\\
&\boldsymbol{C}^{\mathrm{SD}}_{0} = (1 - D_{0n+1})\boldsymbol{C}^{\mathrm{S}}_{0},\\
&\bar{\boldsymbol{\sigma}}_{n+1} = v_0\left(1 - D_{0n+1}\right)\hat{\boldsymbol{\sigma}}_{0n+1} + v_{\mathrm{I}}\hat{\boldsymbol{\sigma}}_{\mathrm{I}n+1}\,.
\end{aligned} \tag{15}$$

2.2.3 | Phase constitutive behavior

Finally, the phase responses obey the damage-enhanced elasto-plastic law:

$$\begin{aligned}
&\hat{\boldsymbol{\sigma}}_i(t) = \hat{\boldsymbol{\sigma}}_i\left(\boldsymbol{\varepsilon}_i(t); \boldsymbol{q}(\tau)\right), \tau \in [0, t])\\
&D_i(t) = D_i\left(\boldsymbol{\varepsilon}_i(t); \boldsymbol{q}(\tau), \tilde{\boldsymbol{q}}(\tau)\right), \tau \in [0, t]),
\end{aligned} \tag{16}$$

where $\boldsymbol{q}$ is a set of internal variables and $\tilde{\boldsymbol{q}}$ is their non-local counterpart used to avoid the mesh dependency of the solution. In the next Section, we specify these expressions in the context of pressure-dependent elasto-plasticity.

3 | PRESSURE SENSITIVE PHASE MATERIAL LAW

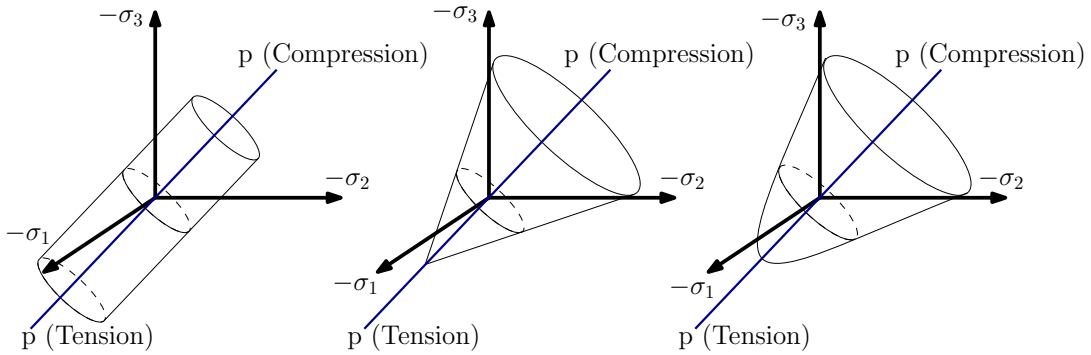

FIGURE 4 Graphical representation of the von Mises (left), the pressure-dependent Drucker-Prager (center) and Nguyen et al.' pressure-sensitive[68] (right) yield surfaces on the stress space.

The Drucker-Prager yield surface model is a well known yield criterion whose yield surface not only varies with respect to the second invariant, but also presents a dependence on the hydrostatic stress, showing a cone-like shaped yield surface (see Fig. 4).

This yield surface was later extended multiple times to represent accurately different material behaviors. This criterion was used by Nguyen et al.[68], who developed a power-enhanced version of this yield surface and applied it to the case of amorphous glassy polymers, developing a hyperelastic viscoelastic-viscoplastic-damage constitutive model based on a multi-mechanism non-local damage continuum. The developed power-enhanced version of the Drucker-Prager is then capable of not only representing materials following a cone-like shape in the stress space, but also more complex power yield surfaces. This model has the capabilities to mimic real epoxy materials like the high-crosslinked RTM6 epoxy resin[69].

In this section, with a view to its embedding in a MFH scheme, this power-enhanced yield condition version of the Drucker-Prager criterion is implemented in an incremental-secant approach for elasto-plastic and damage enhanced cases. For the sake of conciseness, the subscript referring to the phase is omitted.

3.1 | Pressure-dependent model

The Drucker-Prager yield function consists of a linear combination of the two first invariants, making it dependent on the hydrostatic pressure. Nguyen et al. enhanced this model by adding an exponent ($\alpha \geq 1$) in the octahedral term. Considering that the plastic flow is written in the effective stress space in case of damage, the yield criterion reads:

$$f\left(\hat{\boldsymbol{\sigma}}, p\right) = \frac{\left((\hat{\boldsymbol{\sigma}})^{\mathrm{eq}}\right)^{\alpha}}{\sigma_c^{\alpha}} - 3\frac{m^{\alpha}-1}{(m+1)\sigma_c}\hat{\phi} - \frac{m^{\alpha}+m}{m+1} \leq 0, \tag{17}$$

where the superscript "eq" stands for the equivalent von Mises effective stress, $\hat{\phi} = 1/3\,\mathrm{tr}(\hat{\boldsymbol{\sigma}})$, σ_c represents the current compressive yield stress and $m = \frac{\sigma_t}{\sigma_c}$ is the ratio between the current tensile and compressive yield stresses. With a view to the damage-enhanced case, the yield surface is written in the effective space.

The exponent α observed in the first term of the yield criterion allows recovering different power yield surfaces. It is possible to observe that when α is set to one, the classical Drucker-Prager yield criterion is recovered. For the case in which a value of $\alpha = 2$ is used, the paraboloidal yield surface studied by Merlo et al.[70] is recovered. The ratio between the current yield stresses permits to model the effect of a tension-compression flow asymmetry.

In order to correctly capture the complex behavior of polymers, the use of a non-associated flow rule is normally integrated (Abu Al-Rub et al.[80]; Melro et al.[70]; Vogler et al.[81]). This means that, contrary to the case of an associate flow rule in which the plastic flow evolves taking into account the gradient of the yield function, the non-associated flow rule follows a direction normal to a plastic flow potential. In this work, as in Nguyen et al.[68], a quadratic flow potential is used in order to be able to control the Poisson ratio during the plastic process. This plastic flow potential is written as[70]:

$$g = \left(\hat{\boldsymbol{\sigma}}^{\mathrm{eq}}\right)^2 + \beta\hat{\phi}^2, \tag{18}$$

where β is a material parameter. This flow potential permits modeling the volumetric plastic deformation with what is called a plastic Poisson ratio. At the plastic flow onset, the plastic Poisson ratio writes:

$$\nu_p = \frac{9-2\beta}{18+2\beta}. \tag{19}$$

This combination of the modified Drucker-Prager yield surface coupled with the use of the flow potential described by Melro et al.[70] was proven to yield satisfactory results and to be able of accurately representing the pressure-dependent plastic behavior of highly crosslinked epoxies such as the RTM6 in previous works, and allows to easily match a wide variety of pressure-dependent behaviors thanks to the modifications applied to the original criterion. This flexibility and proven performance made this an ideal option for this paper and future implementations of this scheme.

The direction of the flow is then defined as $\mathbf{N} = \frac{\partial g}{\partial \hat{\boldsymbol{\sigma}}}$ and can be evaluated[68] as:

$$\mathbf{N} = \frac{\partial g}{\partial \hat{\boldsymbol{\sigma}}} = 3\hat{\boldsymbol{\sigma}}^{\mathrm{dev}} + \frac{2\beta}{3}\hat{\boldsymbol{\sigma}}^{\mathrm{vol}}, \tag{20}$$

where $\hat{\boldsymbol{\sigma}}^{\mathrm{vol}} = \hat{\phi}\mathbf{1}$, with "vol"standing for the volume operator $(\bullet)^{\mathrm{vol}} = \frac{1}{3}\mathrm{tr}(\bullet)\mathbf{1}$ with $\mathbf{1}$ being the second order identity tensor and where "dev" stands for the deviatoric operator $(\bullet)^{\mathrm{dev}} = \bullet - (\bullet)^{\mathrm{vol}}$.

The plastic flow evolution can be written as:

$$\dot{\boldsymbol{\varepsilon}}^{\mathrm{pl}} = \dot{\Gamma}\mathbf{N}, \tag{21}$$

where Γ is related to the equivalent plastic strain rate as:

$$\dot{p} = k\sqrt{\dot{\boldsymbol{\varepsilon}}^{\mathrm{pl}} : \dot{\boldsymbol{\varepsilon}}^{\mathrm{pl}}} = k\dot{\Gamma}\sqrt{\boldsymbol{N} : \boldsymbol{N}}; \tag{22}$$

and[70]

$$k = \frac{1}{\sqrt{1+2\nu_p^2}} \quad ; \quad k = \sqrt{\frac{2}{3}} \quad \text{if incompressible flow rule.} \tag{23}$$

3.2 | Residual incremental-secant pressure-dependent model implementation

This section frames this pressure-dependent model into the incremental-secant framework step by step. First the elastic trial is developed, following with the radial return mapping used for the plastic process, finishing with the definition of the secant tensors.

3.2.1 | Elastic trial

First, an elastic flow is assumed to compute a trial effective stress tensor $\boldsymbol{\sigma}_{n+1}$. Using the relations developed in Section 2.2, the trial effective stress tensor reads:

$$\hat{\boldsymbol{\sigma}}^{\mathrm{tr}}_{n+1} = \hat{\boldsymbol{\sigma}}_n + \boldsymbol{C}^{\mathrm{el}} : \Delta\boldsymbol{\varepsilon}_{n+1} = \hat{\boldsymbol{\sigma}}_n + \boldsymbol{C}^{\mathrm{el}} : \left(\Delta\boldsymbol{\varepsilon}^{\mathrm{r}}_{n+1} + \boldsymbol{\varepsilon}^{\mathrm{res}}_n - \boldsymbol{\varepsilon}_n\right) = \hat{\boldsymbol{\sigma}}^{\mathrm{res}}_n + \boldsymbol{C}^{\mathrm{el}} : \Delta\boldsymbol{\varepsilon}^{\mathrm{r}}_{n+1}, \tag{24}$$

where the elastic operator $\boldsymbol{C}^{\mathrm{el}}$, being isotropic, can be expressed in terms of its volumetric and deviatoric components as:

$$\boldsymbol{C}^{\mathrm{el}} = 3\kappa^{\mathrm{el}}\boldsymbol{I}^{\mathrm{vol}} + 2\mu^{\mathrm{el}}\boldsymbol{I}^{\mathrm{dev}}, \tag{25}$$

where the volume and deviatoric fourth order tensors write $\boldsymbol{I}^{\mathrm{vol}} \equiv \frac{1}{3}\mathbf{1}\otimes\mathbf{1}$ and $\boldsymbol{I}^{\mathrm{dev}} = \boldsymbol{I} - \boldsymbol{I}^{\mathrm{vol}}$, κ^{el} is the elastic compressibility modulus and μ^{el} is the elastic shear modulus.

The pressure-sensitive yield criterion is then verified to check whether an elastic or a plastic flow is occurring, with

$$f^{\mathrm{tr}}\left(\hat{\boldsymbol{\sigma}}^{\mathrm{tr}}_{n+1}, p_n\right) = \frac{\left(\left(\hat{\boldsymbol{\sigma}}^{\mathrm{tr}}_{n+1}\right)^{\mathrm{eq}}\right)^{\alpha}}{\sigma_c^{\alpha}} - 3\frac{m^{\alpha}-1}{(m+1)\sigma_c}\hat{\phi}^{\mathrm{tr}}_{n+1} - \frac{m^{\alpha}+m}{m+1} \leq 0, \tag{26}$$

where $\boldsymbol{\sigma}_c = \boldsymbol{\sigma}_c^0 + R(p)$ where p is the accumulated plastic strain and $R(p)$ the hardening law in terms of p. In this work, the ratio $\frac{\sigma_t}{\sigma_c}$ is considered to be constant during the hardening, and the hardening law is defined with respect to the compressive behavior.

If the yield criterion is fulfilled, then the trial effective stress $\hat{\boldsymbol{\sigma}}^{\mathrm{tr}}_{n+1} = \hat{\boldsymbol{\sigma}}_{n+1}$, $p_{n+1} = p_n$ and the secant operator $\boldsymbol{C}^{\mathrm{Sr}} = \boldsymbol{C}^{\mathrm{el}}$.

3.2.2 | Radial return mapping

If the yield criterion is not fulfilled ($f^{\mathrm{tr}} > 0$), a plastic correction must be applied:

$$\hat{\boldsymbol{\sigma}}_{n+1} = \hat{\boldsymbol{\sigma}}^{\mathrm{tr}}_{n+1} - \boldsymbol{C}^{\mathrm{el}} : \Delta\boldsymbol{\varepsilon}^{\mathrm{p}}. \tag{27}$$

Following Wu et al.[47,48], the normal direction shown in Eq. (20) is modified as:

$$\mathbf{N}_{n+1} = 3\left(\boldsymbol{C}^{\mathrm{Sr}} : \Delta\boldsymbol{\varepsilon}^{\mathrm{r}}_{n+1}\right)^{\mathrm{dev}} + \frac{2\beta}{3}\left(\boldsymbol{C}^{\mathrm{Sr}} : \Delta\boldsymbol{\varepsilon}^{\mathrm{r}}_{n+1}\right)^{\mathrm{vol}} = 3\left(\hat{\boldsymbol{\sigma}}_{n+1} - \hat{\boldsymbol{\sigma}}^{\mathrm{res}}_n\right)^{\mathrm{dev}} + \frac{2\beta}{3}\left(\hat{\boldsymbol{\sigma}}_{n+1} - \hat{\boldsymbol{\sigma}}^{\mathrm{res}}_n\right)^{\mathrm{vol}}. \tag{28}$$

This expression corresponds to a first order approximation of the normal direction in the stress space in terms of $\Delta\boldsymbol{\varepsilon}$. As discussed by Wu et al.[82], for infinitesimal strain increments $\Delta\boldsymbol{\varepsilon} \to 0$ for a single phase material, this expression $\mathbf{N}_{n+1}$ tends to the normal of the yield surface. At the trial state, $\mathbf{N}^{\mathrm{tr}}_{n+1}$ writes:

$$\mathbf{N}^{\mathrm{tr}}_{n+1} = 3\left(\boldsymbol{C}^{\mathrm{el}} : \Delta\boldsymbol{\varepsilon}^{\mathrm{r}}_{n+1}\right)^{\mathrm{dev}} + \frac{2\beta}{3}\left(\boldsymbol{C}^{\mathrm{el}} : \Delta\boldsymbol{\varepsilon}^{\mathrm{r}}_{n+1}\right)^{\mathrm{vol}} = 3\left(\hat{\boldsymbol{\sigma}}^{\mathrm{tr}}_{n+1} - \hat{\boldsymbol{\sigma}}^{\mathrm{res}}_n\right)^{\mathrm{dev}} + \frac{2\beta}{3}\left(\hat{\boldsymbol{\sigma}}^{\mathrm{tr}}_{n+1} - \hat{\boldsymbol{\sigma}}^{\mathrm{res}}_n\right)^{\mathrm{vol}}. \tag{29}$$

Since $\boldsymbol{C}^{\mathrm{el}}$ is isotropic, $\boldsymbol{C}^{\mathrm{el}} : \Delta\boldsymbol{\varepsilon}^{p} = \left(3\kappa^{\mathrm{el}}\boldsymbol{I}^{\mathrm{vol}} + 2\mu^{\mathrm{el}}\boldsymbol{I}^{\mathrm{dev}}\right) : \Delta\boldsymbol{\varepsilon}^{p}$, where the plastic strain increment reads:

$$\Delta\boldsymbol{\varepsilon}^{p} = \Gamma\boldsymbol{N}, \tag{30}$$

with the plastic multiplier Γ related to the increment in accumulated plastic strain deformation as:

$$\Delta p = k\Gamma\sqrt{\boldsymbol{N} : \boldsymbol{N}} = k\Gamma\sqrt{6\left(\left(\hat{\boldsymbol{\sigma}}_{n+1} - \hat{\boldsymbol{\sigma}}^{\mathrm{res}}_n\right)^{\mathrm{eq}}\right)^2 + \frac{4}{3}\beta^2\left(\hat{\phi}_{n+1} - \hat{\phi}^{\mathrm{res}}_n\right)^2}. \tag{31}$$

Decomposing the normal into its deviatoric and volumetric parts ($\boldsymbol{N}_{n+1} = \boldsymbol{N}^{\text{dev}}_{n+1} + \boldsymbol{N}^{\text{vol}}_{n+1}$) and following the developments in[68] one can rewrite the plastic correction (27) as:

$$\left(\hat{\boldsymbol{\sigma}}_{n+1}\right)^{\text{dev}} = \left(\hat{\boldsymbol{\sigma}}^{\text{tr}}_{n+1}\right)^{\text{dev}} - 2\mu^{\text{el}}\Gamma\boldsymbol{N}^{\text{dev}}_{n+1}, \text{ and} \tag{32}$$

$$\left(\hat{\boldsymbol{\sigma}}_{n+1}\right)^{\text{vol}} = \left(\hat{\boldsymbol{\sigma}}^{\text{tr}}_{n+1}\right)^{\text{vol}} - 3\kappa^{\text{el}}\Gamma\boldsymbol{N}^{\text{vol}}_{n+1}, \text{ or} \tag{33}$$

$$\hat{\phi}_{n+1} = \hat{\phi}^{\text{tr}}_{n+1} - 3\kappa^{\text{el}}\Gamma\frac{2\beta}{3}\left(\hat{\phi}_{n+1} - \hat{\phi}^{\text{res}}_{n+1}\right). \tag{34}$$

Eqs. (32) and (33) can also be written as:

$$\left(\hat{\boldsymbol{\sigma}}_{n+1} - \hat{\boldsymbol{\sigma}}^{\text{res}}_{n}\right)^{\text{dev}} = \left(\hat{\boldsymbol{\sigma}}^{\text{tr}}_{n+1} - \hat{\boldsymbol{\sigma}}^{\text{res}}_{n}\right)^{\text{dev}} - 2\mu^{\text{el}}\Gamma\boldsymbol{N}^{\text{dev}}_{n+1}, \text{ and} \tag{35}$$

$$\left(\hat{\boldsymbol{\sigma}}_{n+1} - \hat{\boldsymbol{\sigma}}^{\text{res}}_{n}\right)^{\text{vol}} = \left(\hat{\boldsymbol{\sigma}}^{\text{tr}}_{n+1} - \hat{\boldsymbol{\sigma}}^{\text{res}}_{n}\right)^{\text{vol}} - 3\kappa^{\text{el}}\boldsymbol{N}^{\text{vol}}_{n+1}. \tag{36}$$

Using Eq. (28), these two equations are respectively rewritten:

$$\left(\hat{\boldsymbol{\sigma}}_{n+1} - \hat{\boldsymbol{\sigma}}^{\text{res}}_{n}\right)^{\text{dev}} = \left(\hat{\boldsymbol{\sigma}}^{\text{tr}}_{n+1} - \hat{\boldsymbol{\sigma}}^{\text{res}}_{n}\right)^{\text{dev}} - 2\mu^{\text{el}}\Gamma\left(3\left(\hat{\boldsymbol{\sigma}}_{n+1} - \hat{\boldsymbol{\sigma}}^{\text{res}}_{n}\right)^{\text{dev}}\right) = \frac{\left(\hat{\boldsymbol{\sigma}}^{\text{tr}}_{n+1} - \hat{\boldsymbol{\sigma}}^{\text{res}}_{n}\right)^{\text{dev}}}{1 + 6\mu^{\text{el}}\Gamma}, \text{ and} \tag{37}$$

$$\left(\hat{\boldsymbol{\sigma}}_{n+1} - \hat{\boldsymbol{\sigma}}^{\text{res}}_{n}\right)^{\text{vol}} = \left(\hat{\boldsymbol{\sigma}}^{\text{tr}}_{n+1} - \hat{\boldsymbol{\sigma}}^{\text{res}}_{n}\right)^{\text{vol}} - 3\kappa^{\text{el}}\Gamma\left(\frac{2\beta}{3}\left(\hat{\boldsymbol{\sigma}}_{n+1} - \hat{\boldsymbol{\sigma}}^{\text{res}}_{n}\right)^{\text{vol}}\right) = \frac{\left(\hat{\boldsymbol{\sigma}}^{\text{tr}}_{n+1} - \hat{\boldsymbol{\sigma}}^{\text{res}}_{n}\right)^{\text{vol}}}{\left(1 + 2\kappa^{\text{el}}\Gamma\beta\right)}. \tag{38}$$

It is then possible to use Eqs. (37) and (38) to find the relation between $\boldsymbol{N}_{n+1}$, Eq. (28), and $\boldsymbol{N}^{\text{tr}}_{n+1}$, Eq. (29), which writes:

$$\boldsymbol{N}_{n+1} = 3\frac{\left(\hat{\boldsymbol{\sigma}}^{\text{tr}}_{n+1} - \hat{\boldsymbol{\sigma}}^{\text{res}}_{n}\right)^{\text{dev}}}{1 + 6\mu^{\text{el}}\Gamma} + \frac{2\beta}{3}\frac{\left(\hat{\boldsymbol{\sigma}}^{\text{tr}}_{n+1} - \hat{\boldsymbol{\sigma}}^{\text{res}}_{n}\right)^{\text{vol}}}{\left(1 + 2\kappa^{\text{el}}\Gamma\beta\right)}, \tag{39}$$

or when separated into their deviatoric and volumetric terms:

$$\boldsymbol{N}^{\text{dev}}_{n+1} = \frac{1}{1 + 6\mu^{\text{el}}\Gamma}\left(\boldsymbol{N}^{\text{tr}}_{n+1}\right)^{\text{dev}} \quad ; \quad \boldsymbol{N}^{\text{vol}}_{n+1} = \frac{1}{1 + 2\kappa^{\text{el}}\Gamma\beta}\left(\boldsymbol{N}^{\text{tr}}_{n+1}\right)^{\text{vol}}. \tag{40}$$

At this stage, the pressure-sensitive yield criterion is rewritten as:

$$f\left(\hat{\boldsymbol{\sigma}}\right) = \left(\frac{\left(\hat{\boldsymbol{\sigma}}_{n+1} - \hat{\boldsymbol{\sigma}}^{\text{res}}_{n} + \hat{\boldsymbol{\sigma}}^{\text{res}}_{n}\right)^{\text{eq}}}{\sigma_c}\right)^{\alpha} - 3\frac{m^{\alpha} - 1}{(m+1)\,\sigma_c}\left(\hat{\phi}_{n+1} - \hat{\phi}^{\text{res}}_{n} + \hat{\phi}^{\text{res}}_{n}\right) - \frac{m^{\alpha} + m}{m+1} = 0. \tag{41}$$

Making use of the Eqs. (37) and (38), since only the deviatoric parts are involved when evaluating the equivalent operator, Eq. (41) can be expressed in terms of $\boldsymbol{\sigma}^{\text{tr}}$, $\boldsymbol{\sigma}^{\text{res}}$ and Γ as:

$$f\left(\hat{\boldsymbol{\sigma}}^{\text{tr}}, \Gamma\right) = \left(\frac{\left(\frac{\hat{\boldsymbol{\sigma}}^{\text{tr}}_{n+1} - \hat{\boldsymbol{\sigma}}^{\text{res}}_{n}}{1 + 6\mu^{\text{el}}\Gamma} + \hat{\boldsymbol{\sigma}}^{\text{res}}_{n}\right)^{\text{eq}}}{\sigma_c}\right)^{\alpha} - 3\frac{m^{\alpha} - 1}{(m+1)\,\sigma_c}\left(\frac{\hat{\phi}^{\text{tr}}_{n+1} - \hat{\phi}^{\text{res}}_{n}}{1 + 2\kappa^{\text{el}}\Gamma\beta} + \hat{\phi}^{\text{res}}_{n}\right) - \frac{m^{\alpha} + m}{m+1} = 0. \tag{42}$$

In order to find the expression of the plastic multiplier Γ, a Newton-Raphson algorithm is used. Using this final expression of the yield criterion (Eq. (42)), the derivative with respect to Γ writes:

$$\frac{df}{d\Gamma} = \left[-\frac{\alpha}{\sigma_c^{\alpha+1}}\frac{\partial R(\Delta p)}{\partial \Delta p}\left(\left(\frac{\hat{\boldsymbol{\sigma}}^{\text{tr}}_{n+1} - \hat{\boldsymbol{\sigma}}^{\text{res}}_{n}}{1 + 6\mu^{\text{el}}\Gamma} + \hat{\boldsymbol{\sigma}}^{\text{res}}_{n}\right)^{\text{eq}}\right)^{\alpha} + 3\frac{m^{\alpha} - 1}{(m+1)\sigma_c^2}\frac{\partial R(\Delta p)}{\partial \Delta p}\left(\frac{\hat{\phi}^{\text{tr}}_{n+1} - \hat{\phi}^{\text{res}}_{n}}{1 + 2\kappa^{\text{el}}\Gamma\beta} + \hat{\phi}^{\text{res}}_{n}\right)\right]\frac{\partial \Delta p}{\partial \Gamma} + \frac{\partial f}{\partial \Gamma}, \tag{43}$$

where, from Eqs. (31, 37, 38), one has:

$$\begin{aligned}\frac{\partial \Delta p}{\partial \Gamma} =& k\sqrt{6\left(\left(\frac{\hat{\boldsymbol{\sigma}}^{\text{tr}}_{n+1} - \hat{\boldsymbol{\sigma}}^{\text{res}}_{n}}{1 + 6\mu^{\text{el}}\Gamma}\right)^{\text{eq}}\right)^2 + \frac{4\beta^2}{3}\left(\frac{\hat{\phi}^{\text{tr}}_{n+1} - \hat{\phi}^{\text{res}}_{n}}{1 + 2\kappa^{\text{el}}\Gamma\beta}\right)^2} \\ &- \frac{k\Gamma}{2\sqrt{6\left(\left(\frac{\hat{\boldsymbol{\sigma}}^{\text{tr}}_{n+1} - \hat{\boldsymbol{\sigma}}^{\text{res}}_{n}}{1 + 6\mu^{\text{el}}\Gamma}\right)^{\text{eq}}\right)^2 + \frac{4\beta^2}{3}\left(\frac{\hat{\phi}^{\text{tr}}_{n+1} - \hat{\phi}^{\text{res}}_{n}}{1 + 2\kappa^{\text{el}}\Gamma\beta}\right)^2}}\left[72\mu^{\text{el}}\frac{\left(\left(\hat{\boldsymbol{\sigma}}^{\text{tr}}_{n+1} - \hat{\boldsymbol{\sigma}}^{\text{res}}_{n}\right)^{\text{eq}}\right)^2}{\left(1 + 6\mu^{\text{el}}\Gamma\right)^3} + \frac{16\beta^3\kappa^{\text{el}}}{3}\frac{\left(\hat{\phi}^{\text{tr}}_{n+1} - \hat{\phi}^{\text{res}}_{n}\right)^2}{\left(1 + 2\kappa^{\text{el}}\Gamma\beta\right)^3}\right],\end{aligned} \tag{44}$$

and

$$\frac{\partial f}{\partial \Gamma} = -\alpha \left(\frac{\left(\frac{\hat{\boldsymbol{\sigma}}^{\mathrm{tr}}_{n+1} - \hat{\boldsymbol{\sigma}}^{\mathrm{res}}_{n}}{1+6\mu^{\mathrm{el}}\Gamma} + \hat{\boldsymbol{\sigma}}^{\mathrm{res}}_{n} \right)^{\mathrm{eq}}}{\sigma_c} \right)^{\alpha-1} \frac{9\mu^{\mathrm{el}} \left(\hat{\boldsymbol{\sigma}}^{\mathrm{tr}}_{n+1} - \hat{\boldsymbol{\sigma}}^{\mathrm{res}}_{n} \right)^{\mathrm{dev}} : \left(\frac{\hat{\boldsymbol{\sigma}}^{\mathrm{tr}}_{n+1} - \hat{\boldsymbol{\sigma}}^{\mathrm{res}}_{n}}{1+6\mu^{\mathrm{el}}\Gamma} + \hat{\boldsymbol{\sigma}}^{\mathrm{res}}_{n} \right)^{\mathrm{dev}}}{\sigma_c \left(1+6\mu^{\mathrm{el}}\Gamma\right)^2 \left(\frac{\hat{\boldsymbol{\sigma}}^{\mathrm{tr}}_{n+1} - \hat{\boldsymbol{\sigma}}^{\mathrm{res}}_{n}}{1+6\mu^{\mathrm{el}}\Gamma} + \hat{\boldsymbol{\sigma}}^{\mathrm{res}}_{n} \right)^{\mathrm{eq}}} + 3\frac{m^{\alpha}-1}{(m+1)\,\sigma_c} \left(\frac{\hat{\phi}^{\mathrm{tr}}_{n+1} - \hat{\phi}^{\mathrm{res}}_{n}}{\left(1+2\kappa^{\mathrm{el}}\Gamma\beta\right)^2} 2\kappa^{\mathrm{el}}\beta \right). \tag{45}$$

Finally, the algorithmic operator $\boldsymbol{C}^{\mathrm{alg}} = \frac{\partial \boldsymbol{\sigma}}{\partial \boldsymbol{\epsilon}}$ is given in Appendix A.

3.2.3 | Radial return mapping neglecting the residual stress

In the case in which the residual stress is neglected when defining the LCC, see Section 2.2, the normal direction shown in Eq. (20) is the classical direction:

$$\mathbf{N}_{n+1} = 3\left(\hat{\boldsymbol{\sigma}}_{n+1}\right)^{\mathrm{dev}} + \frac{2\beta}{3}\left(\hat{\boldsymbol{\sigma}}_{n+1}\right)^{\mathrm{vol}}. \tag{46}$$

At the trial state, $\mathbf{N}^{\mathrm{tr}}_{n+1}$ writes:

$$\mathbf{N}^{\mathrm{tr}}_{n+1} = 3\left(\hat{\boldsymbol{\sigma}}^{\mathrm{tr}}_{n+1}\right)^{\mathrm{dev}} + \frac{2\beta}{3}\left(\hat{\boldsymbol{\sigma}}^{\mathrm{tr}}_{n+1}\right)^{\mathrm{vol}}. \tag{47}$$

The plastic multiplier Γ is therefore related to the increment in accumulated plastic strain deformation as:

$$\Delta p = k\Gamma\sqrt{\boldsymbol{N} : \boldsymbol{N}} = k\Gamma\sqrt{6\left(\left(\hat{\boldsymbol{\sigma}}_{n+1}\right)^{\mathrm{eq}}\right)^2 + \frac{4}{3}\beta^2\left(\hat{\phi}_{n+1}\right)^2}. \tag{48}$$

The relation between $\boldsymbol{N}_{n+1}$ and $\boldsymbol{N}^{\mathrm{tr}}_{n+1}$ neglecting the residual stress writes:

$$\boldsymbol{N}_{n+1} = 3\frac{\left(\hat{\boldsymbol{\sigma}}^{\mathrm{tr}}_{n+1}\right)^{\mathrm{dev}}}{1+6\mu^{\mathrm{el}}\Gamma} + \frac{2\beta}{3}\frac{\left(\hat{\boldsymbol{\sigma}}^{\mathrm{tr}}_{n+1}\right)^{\mathrm{vol}}}{\left(1+2\kappa^{\mathrm{el}}\Gamma\beta\right)}. \tag{49}$$

The pressure-dependent yield criterion is then expressed in terms of $\boldsymbol{\sigma}^{\mathrm{tr}}$, $\boldsymbol{\sigma}^{\mathrm{res}}$ and Γ as: :

$$f\left(\hat{\boldsymbol{\sigma}}^{\mathrm{tr}}, \Gamma\right) = \left(\frac{\left(\frac{\hat{\boldsymbol{\sigma}}^{\mathrm{tr}}_{n+1}}{1+6\mu^{el}\Gamma} \right)^{\mathrm{eq}}}{\sigma_c} \right)^{\alpha} - 3\frac{m^{\alpha}-1}{(m+1)\sigma_c}\left(\frac{\hat{\phi}^{\mathrm{tr}}_{n+1}}{1+2\kappa^{\mathrm{el}}\Gamma\beta} \right) - \frac{m^{\alpha}+m}{m+1} = 0. \tag{50}$$

The plastic multiplier Γ is then computed, as in the case in which the residual is considered, by means of a Newton-Raphson algorithm, with the derivatives following from Eqs. (43, 44, 45) without the residual stress.

The updated expressions when neglecting the residual stress of $\frac{df}{d\Gamma}$, Eq. (43), $\frac{\partial f}{\partial \Gamma}$, Eq. (45), and of $\boldsymbol{C}^{\mathrm{alg}} = \frac{\partial \boldsymbol{\sigma}}{\partial \boldsymbol{\epsilon}}$ are given in Appendix A.

3.2.4 | Definition of the secant operators in the elasto-plastic case

Knowing Γ and therefore $\hat{\boldsymbol{\sigma}}_{n+1}$, $\boldsymbol{C}^{\mathrm{Sr}}$ can be computed using Eqs. (11, 27). Indeed, one has:

$$\Delta\hat{\boldsymbol{\sigma}}^{\mathrm{r}}_{n+1} = \boldsymbol{C}^{\mathrm{Sr}} : \Delta\boldsymbol{\epsilon}^{\mathrm{r}}_{n+1} = \boldsymbol{C}^{\mathrm{el}} : \Delta\boldsymbol{\epsilon}^{\mathrm{r}}_{n+1} - \boldsymbol{C}^{\mathrm{el}} : \Delta\boldsymbol{\epsilon}^{\mathrm{p}} = \boldsymbol{C}^{\mathrm{el}} : \Delta\boldsymbol{\epsilon}^{\mathrm{r}}_{n+1} - 2\mu^{\mathrm{el}}\Gamma\boldsymbol{N}^{\mathrm{dev}}_{n+1} - 3\kappa^{\mathrm{el}}\Gamma\boldsymbol{N}^{\mathrm{vol}}_{n+1}. \tag{51}$$

Using the relation (40) between $\boldsymbol{N}_{n+1}$ and $\boldsymbol{N}^{\mathrm{tr}}_{n+1}$:

$$\Delta\hat{\boldsymbol{\sigma}}^{\mathrm{r}}_{n+1} = \boldsymbol{C}^{\mathrm{el}} : \Delta\boldsymbol{\epsilon}^{\mathrm{r}}_{n+1} - 2\mu^{\mathrm{el}}\Gamma\frac{1}{1+6\mu^{\mathrm{el}}\Gamma}\left(\boldsymbol{N}^{\mathrm{tr}}_{n+1}\right)^{\mathrm{dev}} - 3\kappa^{\mathrm{el}}\Gamma\frac{1}{1+2\kappa^{\mathrm{el}}\Gamma\beta}\left(\boldsymbol{N}^{\mathrm{tr}}_{n+1}\right)^{\mathrm{vol}}, \tag{52}$$

which, using Eq. (29), can be rewritten as:

$$\Delta\hat{\boldsymbol{\sigma}}^{\mathrm{r}}_{n+1} = \boldsymbol{C}^{\mathrm{el}} : \Delta\boldsymbol{\epsilon}^{\mathrm{r}}_{n+1} - \frac{6\mu^{\mathrm{el}}\Gamma}{1+6\mu^{\mathrm{el}}\Gamma}\left(\boldsymbol{C}^{\mathrm{el}} : \Delta\boldsymbol{\epsilon}^{\mathrm{r}}_{n+1}\right)^{\mathrm{dev}} - \frac{2\beta\kappa^{\mathrm{el}}\Gamma}{1+2\kappa^{\mathrm{el}}\Gamma\beta}\left(\boldsymbol{C}^{\mathrm{el}} : \Delta\boldsymbol{\epsilon}^{\mathrm{r}}_{n+1}\right)^{\mathrm{vol}}, \tag{53}$$

or again

$$\Delta\hat{\boldsymbol{\sigma}}^{\mathrm{r}}_{n+1} = \left[\boldsymbol{C}^{\mathrm{el}} - \frac{6\mu^{\mathrm{el}}\Gamma}{1+6\mu^{\mathrm{el}}\Gamma}\left(\boldsymbol{I}^{\mathrm{dev}} : \boldsymbol{C}^{\mathrm{el}}\right) - \frac{2\beta\kappa^{\mathrm{el}}\Gamma}{1+2\kappa^{\mathrm{el}}\Gamma\beta}\left(\boldsymbol{I}^{\mathrm{vol}} : \boldsymbol{C}^{\mathrm{el}}\right)\right] : \Delta\boldsymbol{\epsilon}^{\mathrm{r}}_{n+1}, \tag{54}$$

Having that the effective stress increment is defined as $\Delta\hat{\boldsymbol{\sigma}}^{\mathrm{r}}_{n+1} = \boldsymbol{C}^{\mathrm{Sr}} : \Delta\boldsymbol{\epsilon}^{\mathrm{r}}_{n+1}$, $\boldsymbol{C}^{\mathrm{Sr}}$ is identified to be:

$$\boldsymbol{C}^{\mathrm{Sr}} = \boldsymbol{C}^{\mathrm{el}} - \frac{6\mu^{\mathrm{el}}\Gamma}{1+6\mu^{\mathrm{el}}\Gamma}\left(\boldsymbol{I}^{\mathrm{dev}} : \boldsymbol{C}^{\mathrm{el}}\right) - \frac{2\beta\kappa^{\mathrm{el}}\Gamma}{1+2\kappa^{\mathrm{el}}\Gamma\beta}\left(\boldsymbol{I}^{\mathrm{vol}} : \boldsymbol{C}^{\mathrm{el}}\right). \tag{55}$$

Since $\boldsymbol{C}^{\mathrm{el}}$ is isotropic, so is the residual-incremental-secant operator of the LCC ($\boldsymbol{C}^{\mathrm{Sr}}$) and it is possible to write:

$$\boldsymbol{C}^{\mathrm{el}} = 3\kappa^{\mathrm{el}}\boldsymbol{I}^{\mathrm{vol}} + 2\mu^{\mathrm{el}}\boldsymbol{I}^{\mathrm{dev}};\ \text{and}\ \boldsymbol{C}^{\mathrm{Sr}} = 3\kappa_s^{\mathrm{r}}\boldsymbol{I}^{\mathrm{vol}} + 2\mu_s^{\mathrm{r}}\boldsymbol{I}^{\mathrm{dev}}, \tag{56}$$

where the expressions for κ_s^{r} and μ_s^{r} are respectively:

$$\kappa_s^{r} = \kappa^{\mathrm{el}} - \frac{2\beta\kappa^{el^2}\Gamma}{1+2\kappa^{\mathrm{el}}\Gamma\beta}\quad ;\ \text{and}\quad \mu_s^{r} = \mu^{\mathrm{el}} - \frac{6\mu^{el^2}\Gamma}{1+6\mu^{\mathrm{el}}\Gamma}. \tag{57}$$

This finding means that the isotropic nature of the LCC secant tensors is preserved for the case of non-associated pressure dependent plastic flow, which avoids the need for the isotropization step during the MFH process.

In the case the zero-incremental-secant approach is considered, i.e. when the residual stress is neglected, the zero-incremental-secant operator would be defined by taking into account the residual strain, but neglecting the residual stress, such that $\hat{\boldsymbol{\sigma}}$ would be defined as:

$$\hat{\boldsymbol{\sigma}} = \boldsymbol{C}^{\mathrm{S0}} : \Delta\boldsymbol{\varepsilon}_{n+1}^{\mathrm{r}}, \tag{58}$$

where $\boldsymbol{C}^{\mathrm{S0}}$ writes:

$$\boldsymbol{C}^{\mathrm{S0}} = 3\kappa_s^{0}\boldsymbol{I}^{\mathrm{vol}} + 2\mu_s^{0}\boldsymbol{I}^{\mathrm{dev}}, \tag{59}$$

with the expressions for κ_s^0 and μ_s^0

$$\kappa_s^{0} = \kappa^{\mathrm{el}} - \frac{2\beta\kappa^{el^2}\Gamma}{1+2\kappa^{\mathrm{el}}\Gamma\beta}\quad ;\ \text{and}\quad \mu_s^{0} = \mu^{\mathrm{el}} - \frac{6\mu^{\mathrm{el}^2}\Gamma}{1+6\mu^{\mathrm{el}}\Gamma}. \tag{60}$$

These expressions are similar to Eq. (57), where Γ does not take into account the residual in its definition.

3.2.5 | Definition of the secant operators in the damage-enhanced elasto-plastic case

In the damage-enhanced case, the damage present at the next time step D_{n+1} should now be computed using the chosen non-local damage model. Section 5 particularizes the damage evolution law used in this work. Once the new damage state is known, it is possible to compute the LCC's damage-enhanced residual-incremental-secant operator and the final stress as:

$$\boldsymbol{C}^{\mathrm{SDr}} = \left(1 - D_{n+1}\right)\boldsymbol{C}^{\mathrm{Sr}},\ \text{with} \tag{61}$$

$$\boldsymbol{\sigma}_{n+1} = \left(1 - D_{n+1}\right)\hat{\boldsymbol{\sigma}}_n^{\mathrm{res}} + \boldsymbol{C}^{\mathrm{SDr}} : \Delta\boldsymbol{\varepsilon}_{n+1}^{\mathrm{r}}. \tag{62}$$

Eq. (61) implies that the damaged shear and bulk moduli are then written as:

$$\begin{aligned}\kappa_s^{\mathrm{Dr}} &= (1-D_{n+1})\kappa^{\mathrm{el}} - (1-D_{n+1})\frac{2\beta\kappa^{\mathrm{el}^2}\Gamma}{1+2\kappa^{\mathrm{el}}\Gamma\beta},\\ \mu_s^{\mathrm{Dr}} &= (1-D_{n+1})\mu^{\mathrm{el}} - (1-D_{n+1})\frac{6\mu^{\mathrm{el}^2}\Gamma}{1+6\mu^{\mathrm{el}}\Gamma}.\end{aligned} \tag{63}$$

In the case the zero-incremental-secant approach is used, the damage-enhanced zero-incremental-secant operator and the final stress would write:

$$\boldsymbol{C}^{\mathrm{SD0}} = \left(1 - D_{n+1}\right)\boldsymbol{C}^{\mathrm{S0}},\ \text{with} \tag{64}$$

$$\boldsymbol{\sigma}_{n+1} = \boldsymbol{C}^{\mathrm{SD0}} : \Delta\boldsymbol{\varepsilon}_{n+1}^{\mathrm{r}}. \tag{65}$$

In this case, the damaged shear and bulk moduli, as for the previous case, write:

$$\begin{aligned}\kappa_s^{\mathrm{D0}} &= (1-D_{n+1})\kappa^{\mathrm{el}} - (1-D_{n+1})\frac{2\beta\kappa^{\mathrm{el}^2}\Gamma}{1+2\kappa^{\mathrm{el}}\Gamma\beta},\\ \mu_s^{\mathrm{D0}} &= (1-D_{n+1})\mu^{\mathrm{el}} - (1-D_{n+1})\frac{6\mu^{\mathrm{el}^2}\Gamma}{1+6\mu^{\mathrm{el}}\Gamma}.\end{aligned} \tag{66}$$

In the following section, $\boldsymbol{C}^{\mathrm{S}}$, κ_s, μ_s and $\boldsymbol{C}^{\mathrm{SD}}$, κ_s^{D} and μ_s^{D} respectively stand either for $\boldsymbol{C}^{\mathrm{Sr}}$, Eq. (56), κ_s^{r}, μ_s^{r}, Eq. (57), $\boldsymbol{C}^{\mathrm{SDr}}$, Eq. (61), κ_s^{Dr} and μ_s^{Dr}, Eq. (63), or for $\boldsymbol{C}^{\mathrm{S0}}$, Eq. (59), κ_s^0, μ_s^0, Eq. (60), $\boldsymbol{C}^{\mathrm{SD0}}$, Eq. (64), κ_s^{D0} and μ_s^{D0}, Eq. (66).

4 | MFH RESOLUTION WITHIN A NON-LOCAL FE FRAMEWORK

In this section, a general description of the "first-order moment" based MFH process is presented and then the complete pressure sensitive MFH computation scheme is exposed and detailed step by step.

Making use of non-local damage in the matrix phase, one can write the governing equations of the homogenized material for the interval $\left[t_n, t_{n+1}\right]$ as:

$$\nabla \cdot \bar{\boldsymbol{\sigma}}^T_{n+1} + \bar{\boldsymbol{f}}_{n+1} = \boldsymbol{0}, \tag{67}$$

where $\bar{\boldsymbol{f}}$ stands for the macro-scale body force vector. By using an implicit non-local form of elasto-plasticity, the matrix governing equations are completed by:

$$\tilde{p}_{0_{n+1}} - \nabla \cdot \left(\boldsymbol{c}_{\mathrm{g}} \cdot \nabla \tilde{p}_{0_{n+1}} \right) = p_{0_{n+1}}, \tag{68}$$

where p_0 is a representation of the matrix plastic strain and $\tilde{p}_0$ stands for a representation of the homogenized matrix non-local accumulated plastic strain. In this work, we consider the damage of the matrix phase only since we are interested in accounting for the effect of the pressure-dependent yield surface on the homogenization scheme. The formulation can be extended to account for fiber failure by considering a scalar damage variable in the inclusion phase in order to capture the composite response[79]. As shown by Wu et al.[67], the system of equations composed by Eq. (67) and (68) can be solved by combining a weak finite element form with Newton-Raphson linearization technique. During this Newton-Raphson resolution, the macro-strain increment $\Delta\bar{\boldsymbol{\varepsilon}}_{n+1}$ and the non-local matrix plastic strain $\tilde{p}_{0_{n+1}}$ are since they arise as degrees of freedom from the weak form discretization. The total macro strain tensor $\bar{\boldsymbol{\varepsilon}}_n$ the internal state variables (including p_{0_n}) at the initial state of the time interval are known from the previous time step resolution. The homogenized stress $\bar{\boldsymbol{\sigma}}_{n+1}$ as well as its derivatives are evaluated by the MFH model.

Therefore knowing the macro-strain increment $\Delta\bar{\boldsymbol{\varepsilon}}_{n+1}$, it is possible to compute the strain increment that is seen by the LCC $\Delta\bar{\boldsymbol{\varepsilon}}^{\mathrm{r}}_{n+1}$ (see Section 2.2):

$$\Delta\bar{\boldsymbol{\varepsilon}}^{\mathrm{r}}_{n+1} = \bar{\boldsymbol{\varepsilon}}_n + \Delta\bar{\boldsymbol{\varepsilon}}_{n+1} - \bar{\boldsymbol{\varepsilon}}^{\mathrm{res}}_n. \tag{69}$$

By defining the LCC operators $\boldsymbol{C}^{\mathrm{LCC}}_{\mathrm{I}}$ and $\boldsymbol{C}^{\mathrm{LCC}}_{0}$ making use of the isotropic linear comparison operators $\boldsymbol{C}^{\mathrm{S}}_{\mathrm{I}}$ and $\boldsymbol{C}^{\mathrm{SD}}_{0}$, the MFH process can be summed up by the relation between the phases and composite strains and stresses and the direct relation between the strain phases via a concentration tensor $\boldsymbol{B}^{\epsilon}$:

$$\begin{aligned}
\Delta\bar{\boldsymbol{\varepsilon}}^{\mathrm{r}}_{n+1} &= v_0 \Delta\boldsymbol{\varepsilon}^{\mathrm{r}}_{0n+1} + v_{\mathrm{I}} \Delta\boldsymbol{\varepsilon}^{\mathrm{r}}_{\mathrm{I}n+1}\,, \\
\bar{\boldsymbol{\sigma}}_{n+1} &= v_0 \boldsymbol{\sigma}_{0n+1} + v_{\mathrm{I}} \boldsymbol{\sigma}_{\mathrm{I}n+1}\,, \\
\Delta\boldsymbol{\varepsilon}^{\mathrm{r}}_{\mathrm{I}n+1} &= \boldsymbol{B}^{\epsilon}\left(\mathrm{I}, \boldsymbol{C}^{\mathrm{SD}}_{0}, \boldsymbol{C}^{\mathrm{S}}_{\mathrm{I}}\right) : \Delta\boldsymbol{\varepsilon}^{\mathrm{r}}_{0n+1}.
\end{aligned} \tag{70}$$

The system resolution follows the next steps:

1. In order to solve this set of equations, the strain increment of the inclusions phase is initialized: $\Delta\bar{\boldsymbol{\varepsilon}}^{\mathrm{r}}_{n+1} \rightarrow \Delta\boldsymbol{\varepsilon}^{\mathrm{r}}_{\mathrm{I}n+1}$. Then, the following scheme is solved iteratively:

   (a) The constitutive material law of the inclusions is called and computed using the phase strain increment tensor $\Delta\boldsymbol{\varepsilon}^{\mathrm{r}}_{\mathrm{I}n+1}$ and the current state of the internal variables at the beginning of the iteration. This updates the inclusion phase stress $\boldsymbol{\sigma}_{\mathrm{I}n+1}$, internal variables, incremental-secant operator $\boldsymbol{C}^{\mathrm{Sr}}_{\mathrm{I}_{n+1}}$ and "consistent" anisotropic operator $\boldsymbol{C}^{\mathrm{alg}}_{\mathrm{I}_{n+1}} = \frac{\partial\boldsymbol{\sigma}_{\mathrm{I}_{n+1}}}{\partial\Delta\boldsymbol{\varepsilon}_{\mathrm{I}_{n+1}}}$ reported in Appendix A.

   (b) It is now possible to compute the matrix average strain as:

$$\Delta\boldsymbol{\varepsilon}^{\mathrm{r}}_{0n+1} = \frac{\left(\Delta\bar{\boldsymbol{\varepsilon}}^{\mathrm{r}}_{n+1} - v_{\mathrm{I}}\Delta\boldsymbol{\varepsilon}^{\mathrm{r}}_{\mathrm{I}n+1}\right)}{v_0}\,. \tag{71}$$

   (c) Then, the constitutive material law of the matrix described in Section 3 is called using the strain tensor increment $\Delta\boldsymbol{\varepsilon}^{\mathrm{r}}_{0n+1}$ and the internal state variables at t_n. This gives the updated matrix stress $\boldsymbol{\sigma}_{0n+1}$, damage state $D_{0_{n+1}}$, internal variables and the consistent and incremental-secant operators $\boldsymbol{C}^{\mathrm{alg}}_{0_{n+1}}$, $\boldsymbol{C}^{\mathrm{algD}}_{0_{n+1}} = \left(1 - D_{0_{n+1}}\right)\boldsymbol{C}^{\mathrm{alg}}_{0}$ and $\boldsymbol{C}^{\mathrm{SD}}_{0_{n+1}}$.

   (d) Knowing the matrix incremental-secant operator, the Eshelby tensor $\boldsymbol{S}\left(\mathrm{I}, \boldsymbol{C}^{\mathrm{SD}}_{0_{n+1}}\right)$ is evaluated.

   (e) For the time interval $\left[t_n, t_{n+1}\right]$ the strain increment of the composite material and the non-local plastic strain of the matrix ($\Delta\bar{\boldsymbol{\varepsilon}}^{\mathrm{r}}_{n+1}$ and $\Delta\tilde{p}_{0_{n+1}}$) are known and the stress residual vector $\boldsymbol{F}$ of the system of Eqs. (70), see Appendix B, is evaluated:

$$F = \boldsymbol{C}^{\mathrm{SD}}_{0_{n+1}} : \left[\Delta\boldsymbol{\varepsilon}^{\mathrm{r}}_{\mathrm{I}n+1} - \frac{1}{v_0}\boldsymbol{S}^{-1} : \left(\Delta\boldsymbol{\varepsilon}^{\mathrm{r}}_{\mathrm{I}n+1} - \Delta\bar{\boldsymbol{\varepsilon}}^{\mathrm{r}}_{n+1}\right)\right] - \boldsymbol{C}^{\mathrm{S}}_{\mathrm{I}_{n+1}} : \Delta\boldsymbol{\varepsilon}^{\mathrm{r}}_{\mathrm{I}n+1}\,. \tag{72}$$

(f) The inclusion strain increment is thus corrected following:

$$\Delta\boldsymbol{\varepsilon}^{\mathrm{r}}_{\mathrm{I}_{n+1}} \leftarrow \Delta\boldsymbol{\varepsilon}^{\mathrm{r}}_{\mathrm{I}_{n+1}} - \boldsymbol{J}^{-1} : F, \tag{73}$$

where the Jacobian $\boldsymbol{J}$ is given in Appendix B.

(g) Then, a new iteration is started, going back to step (a) until $|\boldsymbol{F}| \leq$ Tol.

2. Once convergence is reached:

(a) Compute the internal variables and the homogenized stress:

$$\bar{\boldsymbol{\sigma}}_{n+1} = v_0\boldsymbol{\sigma}_{0_{n+1}} + v_{\mathrm{I}}\boldsymbol{\sigma}_{\mathrm{I}_{n+1}}\,. \tag{74}$$

(b) Using the "consistent" tangent operators $\bar{\boldsymbol{C}}^{\mathrm{alg}} = \frac{\partial\bar{\boldsymbol{\sigma}}}{\partial\bar{\boldsymbol{\varepsilon}}}$ and $\boldsymbol{C}_{\tilde{p}} = \frac{\partial\bar{\boldsymbol{\sigma}}}{\partial\tilde{p}_0}$, with

$$\bar{\boldsymbol{C}}^{\mathrm{alg}}_{n+1} = v_{\mathrm{I}}\boldsymbol{C}^{\mathrm{alg}}_{\mathrm{I}} : \frac{\partial\boldsymbol{\varepsilon}_{\mathrm{I}}}{\partial\bar{\boldsymbol{\varepsilon}}} + v_0\left(\boldsymbol{C}^{\mathrm{algD}}_0 - \hat{\boldsymbol{\sigma}}_0\otimes\frac{\partial D_0}{\partial\boldsymbol{\varepsilon}_0}\right) : \frac{\partial\boldsymbol{\varepsilon}_0}{\partial\bar{\boldsymbol{\varepsilon}}}, \text{ and} \tag{75}$$

$$\boldsymbol{C}_{\tilde{p}} = v_{\mathrm{I}}\boldsymbol{C}^{\mathrm{alg}}_{\mathrm{I}} : \frac{\partial\boldsymbol{\varepsilon}_{\mathrm{I}}}{\partial\tilde{p}_0} + v_0\left(\boldsymbol{C}^{\mathrm{algD}}_0 - \hat{\boldsymbol{\sigma}}_0\otimes\frac{\partial D}{\partial\boldsymbol{\varepsilon}_0}\right) : \frac{\partial\boldsymbol{\varepsilon}_0}{\partial\tilde{p}} - v_0\hat{\boldsymbol{\sigma}}_0\frac{\partial D_0}{\partial\tilde{p}_0}, \tag{76}$$

the consistent linearization of the homogenized stress can be computed:

$$\delta\bar{\boldsymbol{\sigma}} = \bar{\boldsymbol{C}}^{\mathrm{alg}} : \delta\bar{\boldsymbol{\varepsilon}} + \boldsymbol{C}_{\tilde{p}}\delta\tilde{p}_0. \tag{77}$$

The expressions of $\boldsymbol{C}^{\mathrm{alg}}_i$ are given in Appendix A, the expressions of $\frac{\partial\boldsymbol{\varepsilon}_i}{\partial\bar{\boldsymbol{\varepsilon}}}$ and $\frac{\partial\boldsymbol{\varepsilon}_i}{\partial\tilde{p}_0}$ are given in Appendix B and the expressions of $\frac{\partial D_0}{\partial\boldsymbol{\varepsilon}_0}$ and $\frac{\partial D_0}{\partial\tilde{p}_0}$ are given in Appendix E.
In order to solve the weak form (67-68), one also needs the linearization of p_0 which writes:

$$\delta p_0 = \frac{\partial p_0}{\partial\bar{\boldsymbol{\varepsilon}}}\delta\bar{\boldsymbol{\varepsilon}} + \frac{\partial p_0}{\partial\tilde{p}_0}\delta\tilde{p}_0, \tag{78}$$

where the derivative of p_0 with respect to the strain is indirectly related to the plastic multiplier, as shown in Eqs. (44) and (31) through

$$\frac{\partial p_0}{\partial\bar{\boldsymbol{\varepsilon}}} = \frac{\partial p_0}{\partial\Gamma_0}\frac{\partial\Gamma_0}{\partial\boldsymbol{\varepsilon}_0}\frac{\partial\boldsymbol{\varepsilon}_0}{\partial\bar{\boldsymbol{\varepsilon}}}, \tag{79}$$

with $\frac{\partial p_0}{\partial\Gamma_0}$ obtained from Eq. (44), $\frac{\partial\Gamma_0}{\partial\boldsymbol{\varepsilon}_0}$ from Appendix A and $\frac{\partial\boldsymbol{\varepsilon}_0}{\partial\bar{\boldsymbol{\varepsilon}}}$ from Appendix B. The derivative $\boldsymbol{C}_p = \frac{\partial p_0}{\partial\tilde{p}_0}$ is given in Appendix A.

3. Then, the unloading step is performed, obtaining the needed composite material, matrix and inclusion phases, residual strains $\left(\bar{\boldsymbol{\varepsilon}}^{\mathrm{res}}_{n+1}, \boldsymbol{\varepsilon}^{\mathrm{res}}_{0_{n+1}}, \text{ and } \boldsymbol{\varepsilon}^{\mathrm{res}}_{\mathrm{I}_{n+1}}\right)$, the inclusions residual stress $\boldsymbol{\sigma}^{\mathrm{res}}_{\mathrm{I}_{n+1}}$ and the matrix phase effective residual stress $\hat{\boldsymbol{\sigma}}^{\mathrm{res}}_{0_{n+1}}$ required for the next loading increment. To this end:

(a) Considering a pure virtual elastic process, the composite material is unloaded up to a zero stress state. The residual strain of the composite is then computed following Eqs. (10), yielding

$$\bar{\boldsymbol{\varepsilon}}^{\mathrm{res}}_{n+1} = \bar{\boldsymbol{\varepsilon}}_{n+1} - \Delta\bar{\boldsymbol{\varepsilon}}^{\mathrm{unload}}_{n+1} = \bar{\boldsymbol{\varepsilon}}_{n+1} - \left(\bar{\boldsymbol{C}}^{\mathrm{elD}}_{n+1}\right)^{-1} : \bar{\boldsymbol{\sigma}}_{n+1}. \tag{80}$$

(b) Once the residual strain of the composite is known, the matrix and inclusion phase residual stresses are computed as:

$$\boldsymbol{\varepsilon}^{\mathrm{res}}_{0_{n+1}} = \boldsymbol{\varepsilon}_{0_{n+1}} - \Delta\boldsymbol{\varepsilon}^{\mathrm{unload}}_{0_{n+1}} = \boldsymbol{\varepsilon}_{0n+1} - \left[v_{\mathrm{I}}\boldsymbol{B}^{\epsilon}(\mathrm{I}, \boldsymbol{C}^{\mathrm{elD}}_0, \boldsymbol{C}^{\mathrm{el}}_{\mathrm{I}}) + v_0\boldsymbol{I}\right]^{-1} : \Delta\bar{\boldsymbol{\varepsilon}}^{\mathrm{unload}}_{n+1}, \text{ and} \tag{81}$$

$$\boldsymbol{\varepsilon}^{\mathrm{res}}_{\mathrm{I}_{n+1}} = \boldsymbol{\varepsilon}_{\mathrm{I}_{n+1}} - \Delta\boldsymbol{\varepsilon}^{\mathrm{unload}}_{\mathrm{I}_{n+1}} = \boldsymbol{\varepsilon}_{\mathrm{I}_{n+1}} - \boldsymbol{B}^{\epsilon}(\mathrm{I}, \boldsymbol{C}^{\mathrm{elD}}_0, \boldsymbol{C}^{\mathrm{el}}_{\mathrm{I}}) : \left[v_{\mathrm{I}}\boldsymbol{B}^{\epsilon}(\mathrm{I}, \boldsymbol{C}^{\mathrm{elD}}_0, \boldsymbol{C}^{\mathrm{el}}_{\mathrm{I}}) + v_0\boldsymbol{I}\right]^{-1} : \Delta\bar{\boldsymbol{\varepsilon}}^{\mathrm{unload}}_{n+1}\,. \tag{82}$$

(c) The residual stress of the inclusion phase and the effective stress of the matrix phase are then computed as:

$$\hat{\boldsymbol{\sigma}}^{\mathrm{res}}_{0_{n+1}} = \hat{\boldsymbol{\sigma}}_{0n+1} - \boldsymbol{C}^{\mathrm{el}}_{0_{n+1}} : \Delta\boldsymbol{\varepsilon}^{\mathrm{unload}}_{0_{n+1}}, \text{ and} \tag{83}$$

$$\boldsymbol{\sigma}^{\mathrm{res}}_{\mathrm{I}_{n+1}} = \boldsymbol{\sigma}_{\mathrm{I}n+1} - \boldsymbol{C}^{\mathrm{el}}_{\mathrm{I}_{n+1}} : \Delta\boldsymbol{\varepsilon}^{\mathrm{unload}}_{\mathrm{I}_{n+1}}\,. \tag{84}$$

5 | VERIFICATION OF THE MFH SCHEME PREDICTION WITH DIRECT FE SIMULATIONS

After developing the incremental-secant implementation of the pressure-dependent model and the MFH scheme used for the homogenization of the two-phase composite with damage in the matrix phase, the MFH model is verified by comparing its predictions to the result obtained through finite-element full-field simulations. The MFH scheme is verified using random UD composite volume element with different volume fractions and spherical inclusions-reinforced matrix considering elastic, elasto-plastic and damage-enhanced phases.

For the direct numerical simulations, we consider a volume element with Periodic Boundary Conditions (PBC), for displacement field and the non-local variables, since it was shown in the work of Nguyen et al.[83] that PBC improves the convergence rate even for non periodic structures. However, when considering failure, multiple localization bands could appear at the failure onset when this kind of boundary condition is used. This is not the case under tensile loading conditions for which this condition is valid, since in those cases the failure band is perpendicular to the loading direction[69]. While remaining out of the onset of localization, the PBC conditions are still valid for all test cases. Another problem after localization onset is the loss of size objectivity and thus the absence of existence of a representative volume element (RVE). In order to recover this size objectivity, a new reference quantity, such as the energy release rate, must be used as a target in order to correctly define the failure stage of the material[84,69]. We note that because of the use of a non-local damage evolution law, MFH is energy consistent during localization since the characteristic length can be evaluated to recover the right amount of dissipated energy during failure[79]. Nevertheless the MFH response during localization cannot be compared to the direct finite element response since the latter depends on the size of the volume element.

In order to be able to mathematically discuss the discrepancies found on the loading test cases, an error measurement scheme is implemented in order to give a more quantitative assessment of the errors found in the MFH predictions on the composite response as well as on the phases responses. To this end, the error on a stress component i is evaluated following:

$$\%\Delta_i = \frac{\int_{\text{Cycle}} \left| \left\langle \sigma_{i_{\text{RVE}}} \right\rangle - \sigma_{i_{\text{MFH}}} \right| d\varepsilon_i}{\int_{\text{Cycle}} \left| \left\langle \sigma_{i_{\text{RVE}}} \right\rangle \right| d\varepsilon_i} \times 100\,, \tag{85}$$

where $\sigma_{i_{\text{RVE}}}$ is the corresponding component of the full-field simulation stress tensor, and $\sigma_{i_{\text{MFH}}}$ stands for the corresponding component of the MFH simulation stress tensor. In order to avoid additive problems, $d\varepsilon_i$ is always taken as positive, including during unloading path. For the phases error, the mean of the inclusion and matrix response errors are considered and added.

5.1 | Matrix and fiber material properties

In this work, two-phase composites are studied. The inclusions phase is modeled as a transversely isotropic elastic material and the matrix as an elasto-plastic, possibly damage-enhanced, material. This phase is modeled with the pressure-dependent-based incremental-secant law introduced in Section 3 using an exponential hardening for the plastic stage of the matrix response:

$$R_0(p_0) = h_0\,(1 - e^{-m_0 p_0})\,. \tag{86}$$

In order to model the damage present in the matrix phase, a two-step model is used in order to model the effective damage evolution within the matrix. This damage law follows a linear damage evolution up to a point referred to as $\bullet_{onset}$, point at which the total accumulated plastic strain and damage are $\widetilde{p}_{onset}$ and $\widetilde{D}_{onset}$. After $\bullet_{onset}$, the law accelerates the damage evolution modeling failure. The resulting law reads

$$\Delta\tilde{D}_0 = \begin{cases} \frac{\widetilde{D}_{onset}}{\widetilde{p}_{onset}} \Delta\widetilde{p}_0, & \text{if} \quad \tilde{p}_0 \leq \tilde{p}_{onset}\,, \\ \frac{\widetilde{D}_{onset}}{\widetilde{p}_{onset}} \Delta\widetilde{p}_0 + \alpha \left(\widetilde{p}_0 + \Delta\widetilde{p}_0 - \widetilde{p}_{\text{onset}}\right)^{\beta} \Delta\widetilde{p}_0, & \text{if} \quad \tilde{p}_0 > \tilde{p}_{onset}. \end{cases} \tag{87}$$

The damage law derivatives are given in Appendix E. This Lemaitre-Chaboche damage formulation in which the damage history is taken into account by means of scalar variables was already used for the modeling of highly cross-linked polymer materials, usually found in composite materials, and proved to be able to represent accurately the damage evolution as well as failure for different test cases, including 3D test with barreling effects[68]. In this latter reference, one scalar damage variable captures the material failure and one scalar damage variables captures the post-peak saturated softening observed under compressive loading.

The two scalar damage variables follow different damage evolution laws and can be reformulated under a single damage variable in a Lemaitre-Chaboche model. Therefore, for the sake of simplicity, we consider a single damage variable in this work.

The properties used for the inclusion phase are the same as the properties used in Nguyen et al.[69] (UD300/CHS carbon fiber) and the matrix properties were chosen so that it matches the RTM6 epoxy resin behavior studied by Nguyen et al.[68]. The inclusions and matrix phases properties are reported in Tables 1, 2 and 3.

TABLE 1 Inclusion phase properties for UD composite.

Inclusions phase properties [Unit]	Value
Longitudinal Young's modulus E_L [GPa]	230
Transverse Young's modulus E_T [GPa]	40
Transverse Poisson ratio ν_{TT} [-]	0.2
Longitudinal transverse Poisson ratio ν_{LT} [-]	0.215
Transverse shear modulus G_{TT} [GPa]	16.7
Longitudinal transverse shear modulus G_{LT} [GPa]	24

TABLE 2 Inclusion phase properties for 3D spherical inclusion reinforced composite.

Inclusions phase properties [Unit]	Value
Young's modulus E [GPa]	230
Poisson ratio ν [-]	0.215

TABLE 3 Matrix phase properties.

Matrix phase properties [Unit]	Value
Young's modulus E_{inf} [MPa]	2450
Poisson ratio ν [-]	0.38
Initial Yield σ_0 [MPa]	48
Yield ratio m [-]	0.85
Initial plastic Poisson's ratio ν_p [-]	0.3
Hardening parameter h_0 [MPa]	164
Hardening parameter m_0 [-]	36.5
Damage parameter $\tilde{p}_{onset}$ [-]	0.14
Damage parameter $\tilde{D}_{onset}$ [-]	0.35
Damage parameter α [-]	18
Damage parameter β [-]	2.5

5.2 | 2D MFH validation with Uni-Directional (UD) composite RVE

In this section, the 2D performance of the developed MFH scheme is studied by comparing the MFH predictions for different volume fractions with its RVE full-field FE simulation counterpart. The elasto-plastic and the damage-enhanced elasto-plastic cases are studied in different test settings, which include uniaxial tension cycles, biaxial tension, shear and non-proportional loading. The considered RVEs are square UD samples of 150 μm, see Fig. 5, generated using the generation process developed by Wu et al.[85]. Three different square RVEs of 150μm side length with different volume fractions were used in order to test

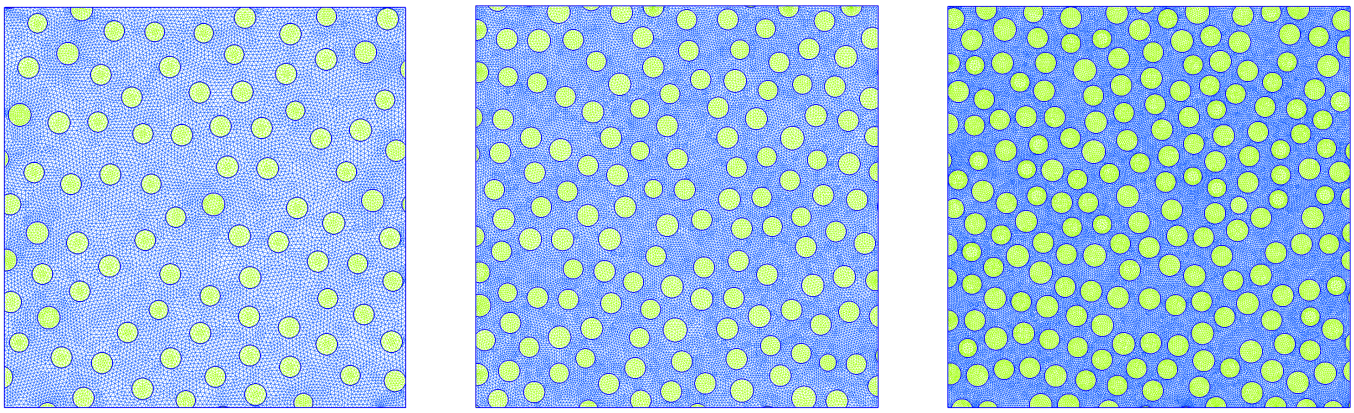

FIGURE 5 18% (left) 28% (center) 40% (right) volume fraction square UD RVE of $150\mu m$ side length with second order mesh. Matrix phase in blue and fiber phase in green.

the MFH capabilities for different volume fractions ranging from 18% to 40%. For the direct FE simulations, the matrix phase considers a non-local matrix $\boldsymbol{c}_g = \text{diag}(l_c^2)$ with $l_c = 3.2\mu m$. All the 2D FE tests were carried out with the third dimension constrained so that plane strain conditions are used.

5.2.1 | Elasto-plastic case

The first verification are made without taking damage into account. As already mentioned, in order to check the validity of the MFH scheme for different levels of volume fractions, three different samples with 18%, 28% and 40% have been tested, see Fig. 5.

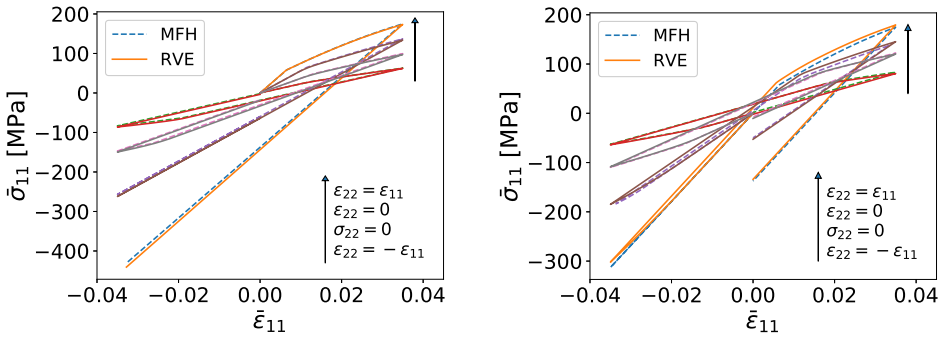

FIGURE 6 Stress-strain curves of tension-compression cycle tests on the elasto-plastic 2D UD sample with 18% inclusion volume fraction. Cycles with different triaxiality levels starting with tension on the left and starting with compression on the right.

Pressure-Dependency test

In order to test the pressure-dependent MFH scheme performance under different hydrostatic pressure conditions, four different strain evolution paths have been used in the two main directions of the 18% RVE. The strain evolution in the 11 direction is kept the same for all the tests while the loading condition in the 22 direction sees different constraints, introducing an added pressure effect in the $\boldsymbol{\varepsilon_{22}} = -\boldsymbol{\varepsilon_{11}}$, $\boldsymbol{\varepsilon_{22}} = \boldsymbol{\varepsilon_{11}}$ and $\boldsymbol{\varepsilon_{22}} = 0$ cases, or keeping the material free to deform in the 22 direction ($\boldsymbol{\sigma}_{22} = 0$). For the 11 direction, two different loading paths are tested, first performing a tension-compression complete cycle, and then a compression-tension complete cycle. The obtained results are shown in Fig. 6.

As Fig. 6 shows, for the tension-compression loading cycle, the MFH scheme is able to accurately capture the behavior of the two-phase composite material for all the tested cases. As it is possible to observe, the pressure-dependent scheme is capable of

predicting correctly the tension-compression flow asymmetry capturing the different behavior of the composite under different hydrostatic pressure conditions. The same is observed in the compression-tension loading cycle. The overall prediction of the MFH model is very satisfactory for all the tested cases.

Volume fraction effect

After testing the pressure-dependency of the model, the effect of the fiber volume fraction is tested for different test cases. The first test performed is a small deformation cyclic uniaxial tension-compression test on the UD composite RVE. The obtained stress-strain curves can be observed in Fig. 7.

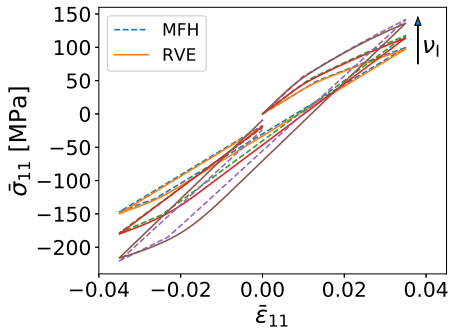

FIGURE 7 Stress-strain curves of the uniaxial tension test on the elasto-plastic 2D UD samples with fiber volume fractions of 18%, 28% and 40%.

TABLE 4 Slopes of the different elastic phases of the uniaxial cycle for the 2D elasto-plastic MFH and Full-Field simulations.

Simulation 18%	**Loading [MPa]**	**Unloading [MPa]**	**Reloading [MPa]**	**Average Slope Error**
Full-Field	3736.72	3736.71	3736.71	
MFH	3707.26	3707.26	3707.26	0.78%
Simulation 28%	**Loading [MPa]**	**Unloading [MPa]**	**Reloading [MPa]**	**Average Slope Error**
Full-Field	4597.38	4599.38	4599.44	
MFH	4527.25	4527.25	4527.25	1.55%
Simulation 40%	**Loading [MPa]**	**Unloading [MPa]**	**Reloading [MPa]**	**Average Slope Error**
Full-Field	5904.17	5908.07	5908.10	
MFH	5634.16	5634.16	5634.16	4.58%

As it can be seen, the MFH predictions yield accurate results for the three volume fractions tested. From Fig. 7 it can be said that the lower the volume fraction the more accurate the MFH prediction is, being the average composite stress predicted by the MFH scheme in the tension stage accurate compared to the finite element simulation. It is possible to observe a slope difference in the elastic phases of the cycle. In order to further investigate this slope difference, we compute the slopes found at each elastic phase of the loading cycle. As Table 4 shows, most of the difference between the full-field simulation and the MFH slope discrepancy can already be found in the first elastic loading stage, which points to the effect of the Mori-Tanaka assumption whose accuracy decreases with the increase of the volume fraction. Besides, even though small-strain constitutive behaviors were used in the FE code, the latter is framed in a finite strain setting, which causes large local deformations to appear in the matrix between two close positioned fibers, and which leads to a slope discrepancy between the elastic loading and elastic unloading phases of the direct numerical simulation.

Fig. 8 shows a more detailed comparison between the MFH prediction and the Full-Field simulation by presenting the averaged stress obtained for each of the phases of the composite with respect to the composite strain evolution. It is possible to observe the good agreement of the matrix phase response, being the lower volume fraction case more accurate than the 40% volume fraction one. A higher discrepancy is found in the fiber phase, in which the slope discrepancy observed in prediction of the composite

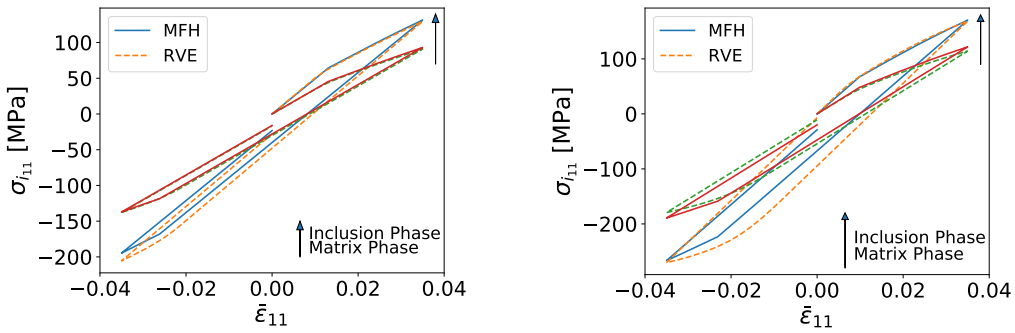

FIGURE 8 Fiber and matrix phase stress - composite strain curves of the uniaxial tension test on the elasto-plastic 2D UD samples with fiber volume fractions of 18% (left) and 40% (right).

response is also seen in this phase prediction. Following the error measurement methodology previously presented, it is possible to have a deeper understanding of the found discrepancies. Table 5 shows that a 1.29% total average error was found for the lowest fiber volume fraction and a 2.895% in the 40% volume fraction case. An averaged total error ranging between 1.9% and 4.33% is found in the detailed phases responses, when increasing the fiber volume fraction. Even though some differences are present as already exposed, they are small enough to conclude that the MFH scheme is capable of satisfactorily predicting the composite behavior.

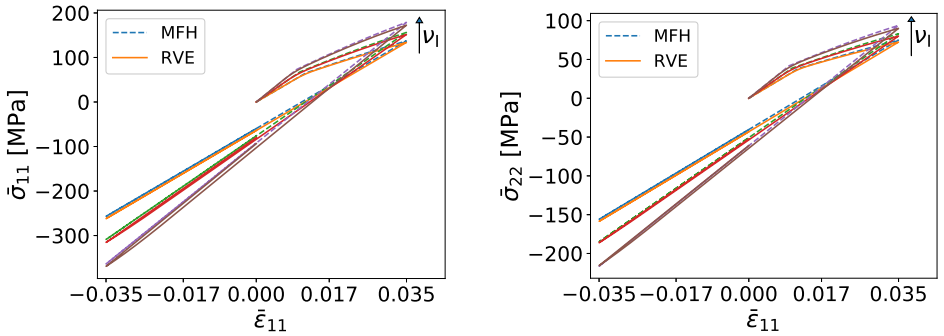

FIGURE 9 Loading and transverse direction stress-strain curves for biaxial loading tests ($\varepsilon_{22} = 0$) on elasto-plastic 2D UD RVE samples with 18, 28 and 40% fiber volume fractions.

The next step in the verification is to perform biaxial tension tests in order to verify the MFH model under different triaxiality conditions. In these biaxial tension tests, the strain in the tension-compression direction 11 is modified while the transverse loading direction 22 remains constant at zero strain ($\varepsilon_{22} = 0$). As in the previous test, RVE with different volume fractions were used in order to test the MFH performance at different volume fractions. The obtained results can be observed in Fig. 9. The MFH shows a good agreement with the obtained responses for all the volume fractions tested and further corroborated by the error values shown in Table 5 for all volume fractions. As in the uniaxial tension test, the higher the volume fraction, the larger the difference in the slope of the unloading/compression phase. The stress in the transverse-loading direction shows how the MFH model is also capable of correctly predicting the behavior of the composite in the 22 direction. The homogenization is therefore capable of predicting a correct composite behavior under different internal pressures showing the pressure-dependence of the simulated material.

Once loading in the two in-plane directions have been studied, shear strain is the next verification step. Shear is a loading condition in which, due to the kind of deformation applied to the composite, when high volume fractions of fibers are present, large deformations in the matrix are observed. As for the previous test, three different RVEs with volume fractions ranging from 18% to 40% were tested in order to assess the performance of the MFH model for different volume fractions. Fig. 10

TABLE 5 Error percentages for different stress components for the 2D elasto-plastic cyclic loading conditions.

Test and volume fraction	Composite 11	Phases 11
Uniaxial; 18%	1.296%	1.901%
Uniaxial; 28%	1.482%	2.184%
Uniaxial; 40%	2.895%	4.334%
	Composite 11	**Phases 11**
Biaxial Cycle; 18%	1.464%	1.764%
Biaxial Cycle; 28%	1.180%	2.765%
Biaxial Cycle; 40%	1.907%	2.745%
	Composite 22	**Phases 22**
Biaxial Cycle; 18%	1.033%	1.114%
Biaxial Cycle; 28%	1.151%	2.32%
Biaxial Cycle; 40%	2.001%	2.094%
	Composite 12	**Phases 12**
Shear Cycle; 18%	1.270%	2.437%
Shear Cycle; 28%	2.037%	2.923%
Shear Cycle; 40%	3.444%	4.812%
	Composite 11	**Phases 11**
Non-proportional $\varepsilon_{22} \neq 0$; 18%	4.380%	4.595%
Non-proportional $\varepsilon_{22} \neq 0$; 40%	8.046%	8.993%
	Composite 12	**Phases 12**
Non-proportional $\varepsilon_{22} \neq 0$; 18%	2.603%	4.129%
Non-proportional $\varepsilon_{22} \neq 0$; 40%	5.634%	7.656%
	Composite 11	**Phases 11**
Non-proportional $\varepsilon_{22} = 0$; 18%	4.656%	4.566%
Non-proportional $\varepsilon_{22} = 0$; 40%	9.088%	9.178%
	Composite 12	**Phases 12**
Non-proportional $\varepsilon_{22} = 0$; 18%	3.056%	5.029%
Non-proportional $\varepsilon_{22} = 0$; 40%	7.136%	7.039%

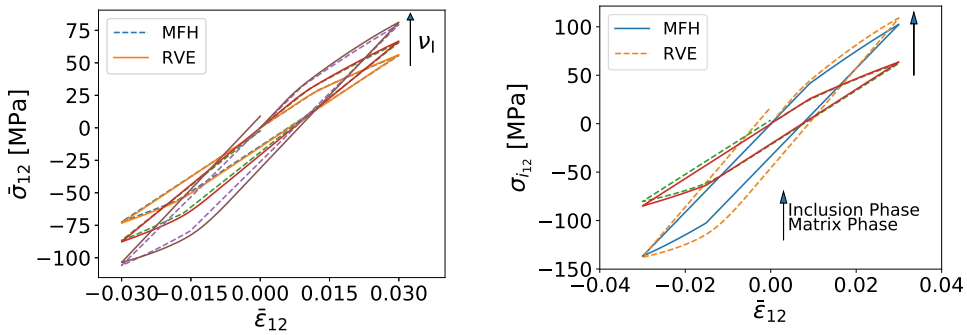

FIGURE 10 Stress-strain curves of shear cycle tests on elasto-plastic 2D UD samples with fiber volume fractions of 18%, 28% and 40% (left) and matrix and fibre phase stress - composite strain curves of the cyclic shear test on the elasto-plastic 2D UD sample with fiber volume fraction of 40% (right).

shows again good MFH predictions of the composite behavior for all three tested RVEs. As in the previous tests, more accurate results are obtained for the lower volume fraction RVEs than for the higher volume fractions. The MFH model shows a slight underestimation of the stress in the first phase of the loading cycle. As for the previous tension tests, the higher the volume

fraction, the higher the difference of the elastic slope in the sample response. Closely studying the responses obtained for each of the phases with respect to the 40% composite strain state shown in Fig. 10, it can be observed how, as for the case of the uniaxial tension test, the matrix phase behavior is correctly captured over the entire path, just showing a small underestimation of the minimum stress reached during the compression phase. This is not the case for the fiber phase, which shows higher discrepancies between the predicted and the full-field response. Most of this discrepancy comes from the fiber phase strain evolution predicted by the MFH, in which the total strain seen by this phase is underestimated compared to the strain observed in the full-field simulation. Detailed error values are reported in Table 5 and one can conclude that the MFH is capable of predicting correctly the behavior of a shear loaded composite with the total average errors remaining below 3.5% for all volume fractions.

Non-proportional loading case

The incremental-secant approach developed by Wu et al.[48] is known for its good accuracy in non-proportional loading. Non-proportional loading conditions on the 18% and 40% RVE is now be tested to see how the implemented incremental-secant pressure-dependent MFH model is capable of predicting the behavior of the composite under this conditions. Two different tests have been performed, in which tension-compression and shear are applied with different loading for the transverse strain direction. The strain evolutions are depicted in Figs. 11 and 12.

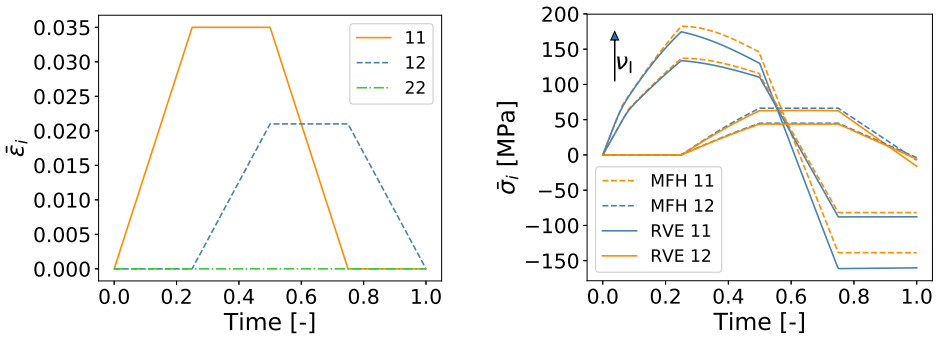

FIGURE 11 Strain-time evolution (left) and stress-time response evolution (right) of 18% and 40% fiber volume fraction elasto-plastic 2D UD samples loaded non-proportionally with $\varepsilon_{22} = 0$.

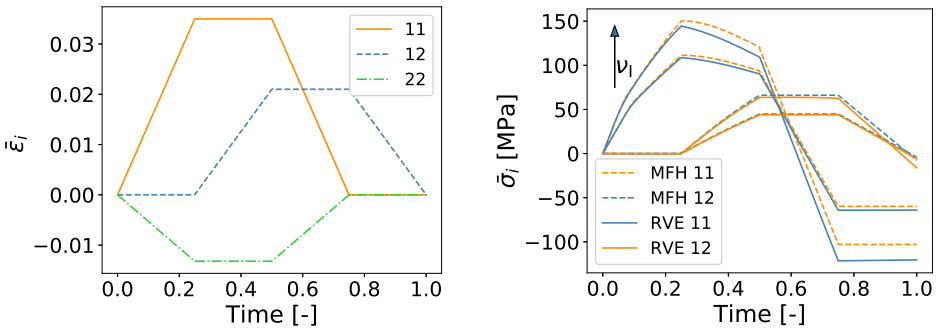

FIGURE 12 Strain-time evolution (left) and stress-time response evolution (right) of 18% and 40% volume fraction elasto-plastic 2D UD samples loaded non-proportionally with $\varepsilon_{22} \neq 0$.

As the results show in Figs. 11 and 12, the MFH model presents a good prediction of the composite behavior shown in the FE simulations. In the first phase of the loading cycle, as already shown in the tension-compression and biaxial tests, a very good agreement between the MFH prediction and the full-field simulation is found for both cases, being the MFH solution slightly stiffer than the full-field one. Then, completing the first half of the test, the shear loading shows a good evolution in both cases for the stress evolution in the longitudinal and shear components. The second half of the test starts by an unloading in the

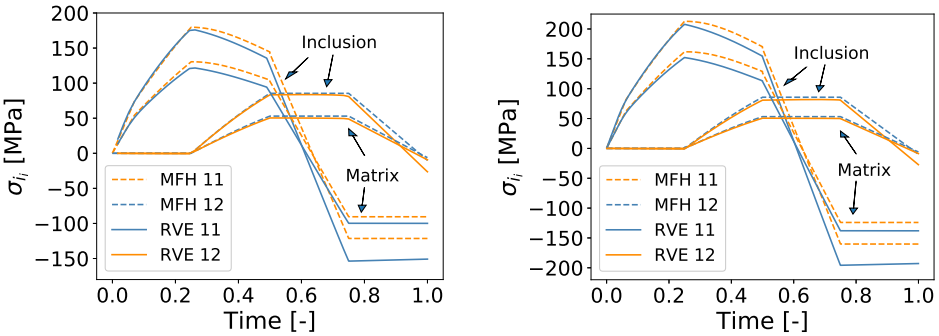

FIGURE 13 Phase stress - time curve of the non-proportional test, with $\varepsilon_{22} \neq 0$ on the left and with $\varepsilon_{22} = 0$ on the right, on the elasto-plastic 2D UD sample with fiber volume fraction of 40%.

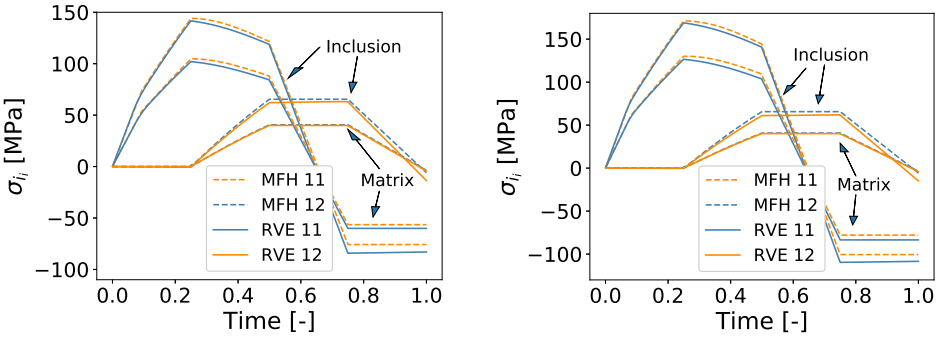

FIGURE 14 Phase stress - time curve of the non-proportional test, with $\varepsilon_{22} \neq 0$ on the left and with $\varepsilon_{22} = 0$ on the right, on the elasto-plastic 2D UD sample with fiber volume fraction of 18%.

longitudinal direction. A small underestimation of the average stress in both components is observed, however, this difference can be considered as relatively small for both components. Finally, in the shear unload phase of the load cycle, one can observe a slight slope difference between the full-field and MFH simulations, being this bigger for the highest volume fraction RVE. Figs. 13 and 14 show a detailed look at each phase behavior for the 18% and 40% volume fraction RVEs on the full-field simulation and the MFH prediction. As in previous cases, the matrix phase behavior is better captured than the inclusion phase, where the largest discrepancies are found during the **11** direction unloading stage after the shear loading. Table 5 shows that although discrepancies are added up during the full loading cycle, these remain reasonable on both, the composite and the phases averaged errors. The general picture for both test cases shows how the pressure-dependent incremental-secant MFH model is capable of performing accurately under non-proportional loading for different triaxiality levels.

5.2.2 | Damage-enhanced elasto-plastic case

The next step is to validate the MFH predictions when accounting for damage-enhanced elasto-plastic phases. All the following tests were performed using periodic boundary conditions for the displacement and for the involved non-local variables and the displacement in the normal direction was constrained so that plane strain conditions are recovered. The 40% volume fraction RVE sample, see Fig. 5, was used in all the tests shown in this section as it is found to be the most challenging case for the MFH model.

Uniaxial and shear loading

In order to test the MFH prediction performance in the damaged-enhanced case, the results for the uniaxial and shear loading are shown herein. When loading the composite up to its failure onset, Fig. 15, it is possible to observe a disagreement between both simulations as the MFH model shows a stiffer behavior when reaching the strain-softening onset, specially in the shear loading case, where a 4.2% difference can be found on the reached maximum stress value. As previously mentioned, the Periodic Boundary Conditions are suitable for all cases while remaining out of the localization onset, but once this onset is reached, the

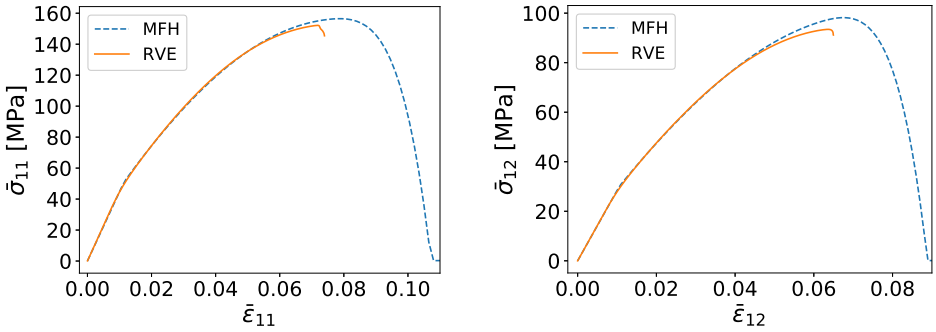

FIGURE 15 Stress-strain curves for the damage-enhanced uniaxial loading test on a 40% 2D UD sample (left), and damage-enhanced shear loading test on a 40% 2D UD sample (right).

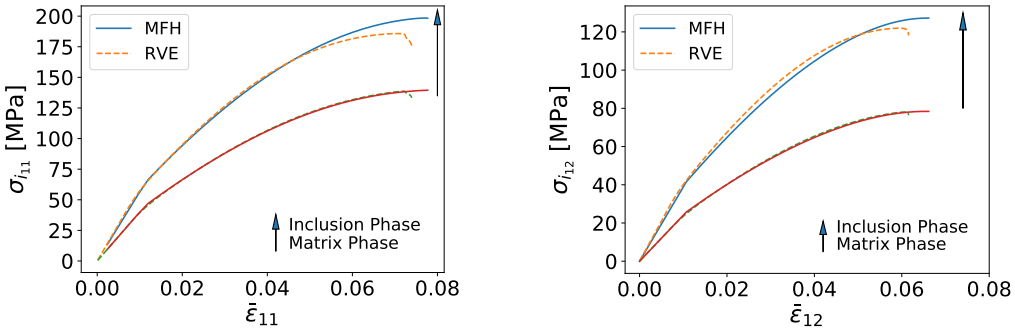

FIGURE 16 Matrix and fiber phase stress - composite strain curves of the uniaxial tension test (left) and shear (right) on the damage-enhanced elasto-plastic 2D UD sample with fiber volume fraction of 40%.

PBC suitability can be degraded in the case of shear loading, as multiple shear bands appear. After this localization onset a loss of size objectivity appears for direct numerical simulation and the results cannot be compared with the MFH which does not suffer from this drawback since the energy dissipation is governed by the non-local characteristic length[79]. Fig. 16 shows a detailed comparison of the phases average stress between the full-field simulation and the MFH prediction. It is possible to observe how the matrix response is correctly captured up to the failure onset, being the difference between both negligible. In the case of the fiber phase, the MFH prediction shows a stiffer behavior when reaching the softening onset on both test cases, however it is possible to conclude that both phases behaviors were correctly represented by the MFH scheme.

Even though a slight slope difference is encountered in the averaged stress evolution in the composite and must be taken into account, one can conclude that the pressure-dependent MFH method is able to correctly predict the composite behavior under a variety of loading conditions including non-proportional loading. A more extensive study accounting for other type of loading conditions such as biaxial loading and non-proportional loading can be found in Appendix F.

5.3 | Spherical inclusions-reinforced matrix

After verifying the accuracy of the MFH scheme in 2D, the MFH methodology is tested in 3D with a matrix reinforced with spherical inclusions. As for the 2D case, cyclic tests is performed in order to assess the accuracy of the MFH methodology in 3D. A 20% volume fraction cubic RVE with around 40 spherical inclusions and 100 μm side length is used, as it was proved to be representative enough of the studied composite. The used RVE can be observed in Fig. 17. As in the 2D case, periodic boundary conditions for the displacement and for the non-local variables involved are used in all the performed tests.

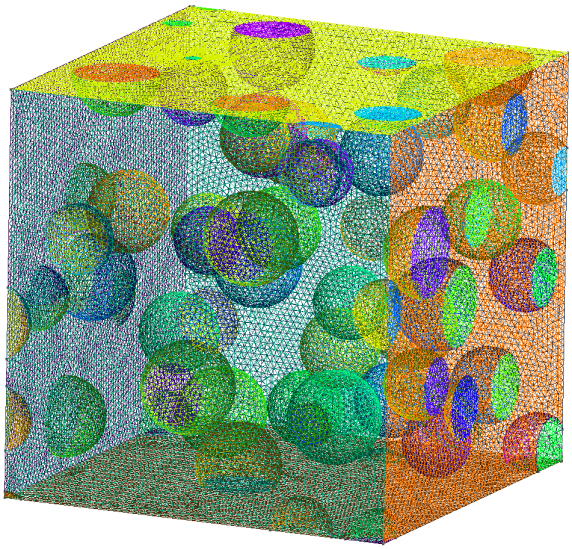

FIGURE 17 3D RVE with 20% spherical inclusions and 100 μm side length meshed with a second order mesh.

5.3.1 | Elasto-plastic case

As for the 2D case, the elasto-plastic case is studied in the first place. This section presents equivalent tests to the ones performed in the UD composite case which allows testing the MFH performance under different conditions, including non-proportional loading.

Uniaxial, triaxial and shear loading

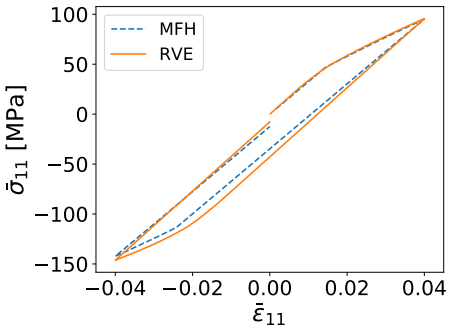

FIGURE 18 Stress-strain curves of a uniaxial tension test on an elasto-plastic 3D RVE with spherical inclusions.

The first test performed is low strain cyclic uniaxial loading. In this test the sample is loaded up to a 4% strain and then symmetrically compressed before returning to a zero-strain state. The obtained results represented in Fig. 18 show a satisfactory prediction of the composite behavior in the entire cycle. The first quarter of the simulation in which the loading is carried out, the stress evolution is correctly captured by the MFH method. Then, in the unloading/compression phase, the slight difference in stress evolution slope already seen in the 2D case is recovered, showing a small underestimation of the absolute stress of the composite. The total errors are reported in Table 6.

In order to check the MFH accuracy under different composite pressure conditions, triaxial loading is now tested. In this test, the sample is strained in the longitudinal direction (11) and the strain in the other two main directions (22 and 33) is set to be constant at zero strain. The obtained results presented in Fig. 19 show a good match between the full-field FE simulations and the MFH prediction with a total error below 2.2% as stated in Table 6. Even though, the difference in slope seen at the

TABLE 6 Error percentages for different stress components for the 3D elasto-plastic cases.

Test and volume fraction	**Composite 11**	**Phases 11**
Uniaxial 20%	2.637%	3.932%
	Composite 11	**Phases 11**
Triaxial 20%	2.142%	2.251%
	Composite 22	**Phases 22**
Triaxial 20%	1.724%	2.195%
	Composite 12	**Phases 12**
Shear low strain 20%	1.014%	1.637%
Shear high strain 20%	1.623%	2.386%
	Composite 11	**Phases 11**
Non-Proportional 20%	4.063%	4.236%
	Composite 12	**Phases 12**
Non-Proportional 20%	3.109%	4.764%

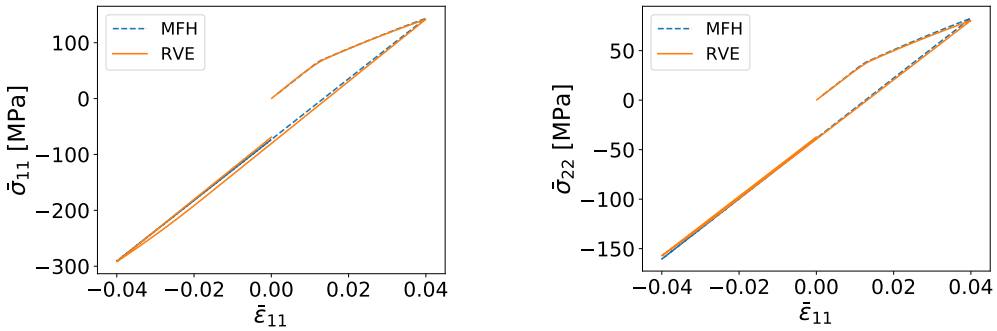

FIGURE 19 11 and 22 direction stress-strain curves of a triaxial loading test on elasto-plastic 3D sample with spherical inclusions.

unloading/compression stage is still observed, this is less pronounced than in the 2D case, and the overall MFH prediction in this 3D case can be considered as accurate.

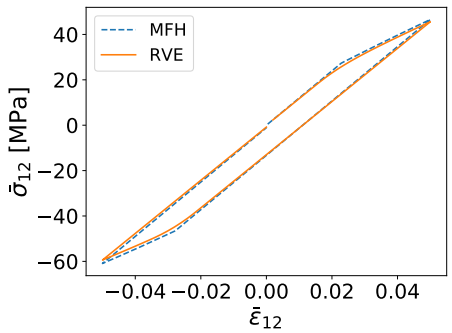

FIGURE 20 Stress-strain curves of a shear cycle test on elasto-plastic 3D RVE with spherical inclusions.

After the uniaxial and triaxial cases have been tested, pure shear loading is tested. The obtained results are shown in Figs. 20 and 21. Fig. 20 shows a good agreement between the full-field simulation and the MFH prediction. As can be observed, with

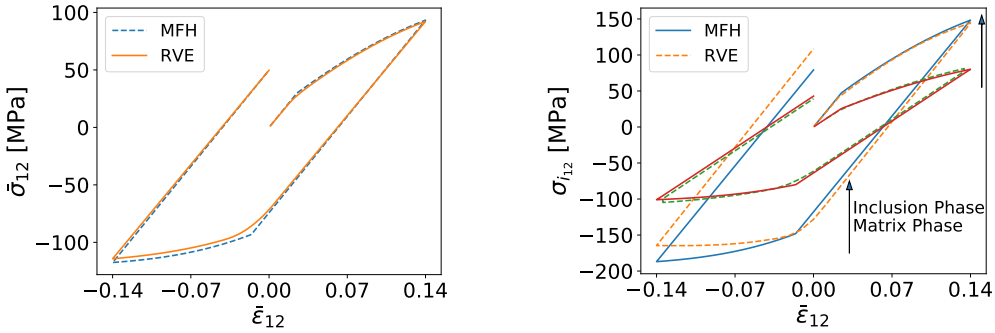

FIGURE 21 Stress-strain curves of a shear cycle tests on elasto-plastic 3D RVE with spherical inclusions (left) and its respective matrix and fibre phase stress - composite strain curves of the shear cycle test on the elasto-plastic 3D sphere-reinforced samples (right).

a full-cycle error of 1% (Table 6), the result is more accurate than the one obtained in the 2D case. Two different shear tests were performed in order to check the performance of the MFH model under different strain percentage conditions. The obtained results show a similar performance for both tests, verifying the correct MFH performance even under higher strain loading paths. Looking at Fig. 21 which shows the obtained responses of each of the phases for the full-field and MFH simulations in the case of the wider shear deformation cycle, once again it is observed a good prediction of the matrix behavior, however a higher difference is found between both simulations for the fiber response, specially in the plastic compressive phase.

Non Proportional Loading

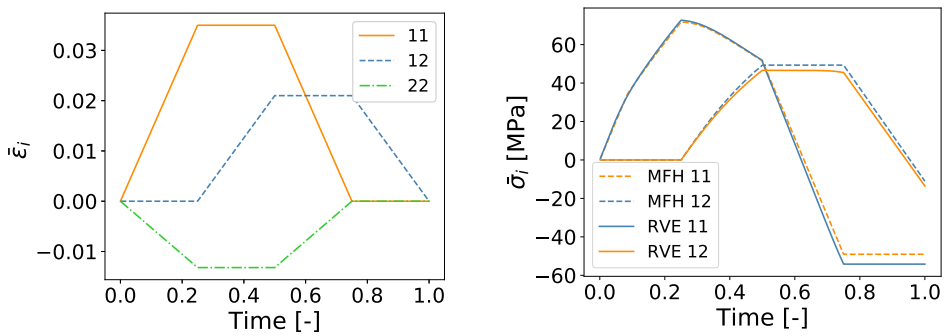

FIGURE 22 11 and 12 component stress-strain curves for a elasto-plastic non-proportional loading test on 3D sample.

Finally, in order to complete the verification of the performance of the MFH model in a three-dimensional case, a non-proportional loading test is performed. Fig. 22 shows the obtained response for the longitudinal and shear components. Fig. 22 shows a satisfactory response prediction for both components. The obtained results, with a full cycle error of about 4.1% for the response in 11, see Table 6, are comparable to those obtained in the 2D case, being the stress of the material slightly overestimated along the entire loading path and finding a small slope difference between the full-field simulation solution and the MFH prediction.

5.3.2 | Damage enhanced elasto-plastic case

When damage was considered in the matrix phase in the 2D case, the MFH method showed a good agreement between its prediction and the full-field FE simulation results. This section now briefly shows the performance of the pressure-sensitive MFH method when damage-enhanced elasto-plasticity is taken into account in the matrix phase of the composite.

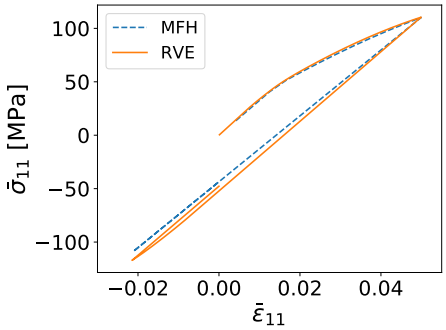

FIGURE 23 Stress-strain curves of a damage-enhanced case of uniaxial loading test on 3D sample.

The first verification test carried out is uniaxial loading, for which the same test as the one performed for the elasto-plastic case is used. As it can be observed in Fig. 23, a good MFH prediction for the performed simulation is seen. The loading path is perfectly captured by the MFH model, following correctly the entire stress evolution. Then, the unloading/compression phase shows a small difference in slope as in the previous cases, which makes the MFH prediction to slightly underestimate the absolute minimum stress reached in the test. However this difference can be seen as negligible as the stress evolution is satisfactorily captured over the complete cycle.

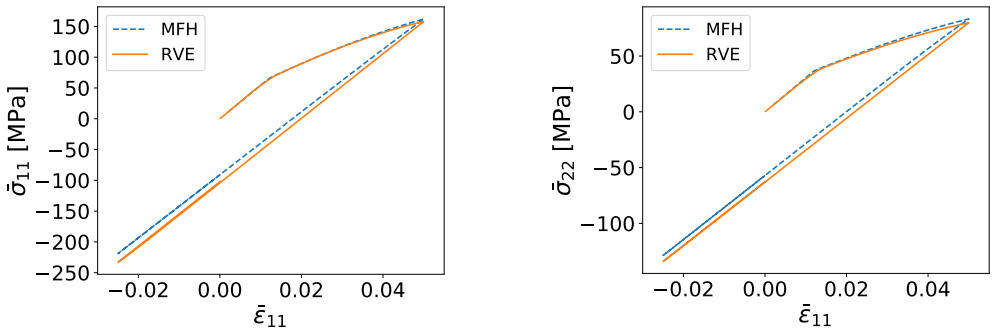

FIGURE 24 11 and 22 component stress-strain curves for a damage-enhanced triaxial loading test on 3D spherical reinforced RVE.

To complete this brief verification of the damage-enhanced 3D case, triaxial loading conditions are taken into account, which allow us to verify the correct performance of the MFH method under different pressure conditions. As illustrated in Fig. 24, this simulation shows a good longitudinal 11 prediction of the stress evolution as for the elasto-plastic case. The transverse direction shows a slight overestimation of the prediction in the loading path, however, this is small enough to consider the MFH prediction as satisfactory.

Table 7 shows how the pressure-dependent MFH method accuratly predicts the damage-enhanced elasto-plastic cases. Similar differences to the ones seen in the 2D case were found, being the slope difference in the unloading-compression phase between the full-field and the MFH simulation smaller than in the 2D case. As for the 2D case, the MFH scheme has shown good accuracy in the 3D case.

TABLE 7 Error percentages for different stress components for the 3D damage-enhanced cases.

Test and volume fraction	**Composite 11**	**Phases 11**
Uniaxial 20%	2.386%	3.932%
	Composite 11	**Phases 11**
Triaxial 20%	4.028%	4.194%
	Composite 22	**Phases 22**
Triaxial 20%	3.274%	3.723%

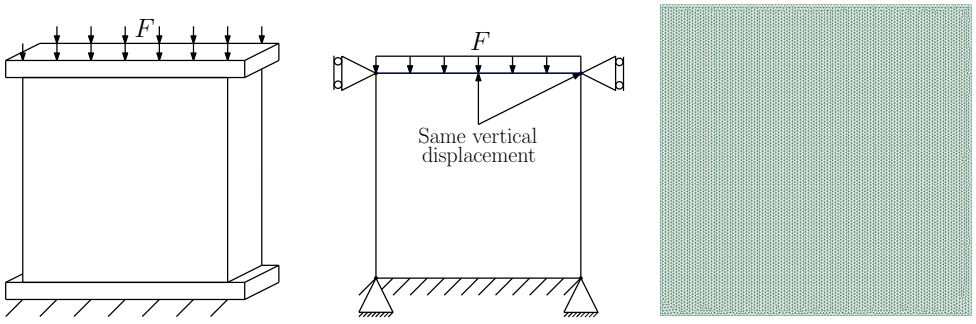

FIGURE 25 Experimental setup used in[71] on the left, boundary conditions in the middle and second-order mesh on the right used for the MFH multi-scale simulation.

6 | EXPERIMENTAL COMPRESSION TEST

Being the performance of the MFH scheme tested at the microscale, in order to complete the MFH validation, a macro-scale transverse compression test is studied. To that end, the compression test performed on a UD composite cube sample by Chevalier et al.[71] is used. For these tests, cubic specimens of UD composite with 10 mm edge length were transversely compressed until reaching failure. In order to simulate this experimental test numerically at an affordable computational cost, a representation of this macro-scale test was performed using a 2D square of 10x10 mm. Fig. 25 shows a comparison between the experimental and numerical setups. For the multi-scale MFH simulation, an unstructured second-order mesh is considered, see Fig.25.

An inclusion volume fraction of 40% is considered since this is the experimentally measured one. The material properties of both phases were identified by Nguyen et al.[69] for visco-elastic-visco-plastic models. Since in the present work we did not consider the viscous effects, in order to recover the same behavior, a correction is applied to the used Young's modulus. The applied correction is computed by considering the instantaneous Young's modulus[68]:

$$E = E_\infty + \sum_{i=1}^{N} E_i \exp\left(\frac{t}{\tau_i}\right), \tag{88}$$

where E_i, $i = \infty, 1..N$, and τ_i, $i = 1..N$ are the modulus and time constants of the N Maxwell branches. Using the parameters identified V.D. Nguyen et al[69], since the elastic part of the experimental test conducted at $\dot{\epsilon} = 10^{-4}s^{-1}$ took place in a time around 150s, the matrix Young's modulus is increased to 2.85 GPa. The other parameters are reported in Table 1 and 3. A non-local length of 80 μm is used in the multi-scale simulation. This non-local value, as well as the post failure onset damage parameters could be calibrated[69] in order to recover the measured experimental energy release rate G_c following the approach set in[79], but this is beyond the objective of the work.

In transverse loading, the matrix dominates the mechanical response of the composite. Fig. 26 shows an accurate prediction of the elasto-plastic behavior of the composite cube, successfully capturing the transition from elasticity to plasticity on the macro-sample as well as representing a similar plastic evolution. The MFH prediction shows a slightly stiffer behavior, when reaching the failure onset, phenomenon that was also observed in the results of Section 5.2.2, however this could be due to the simple damage evolution used in this work, as well as the use of the simplified two dimensional sample coupled with plane strain.

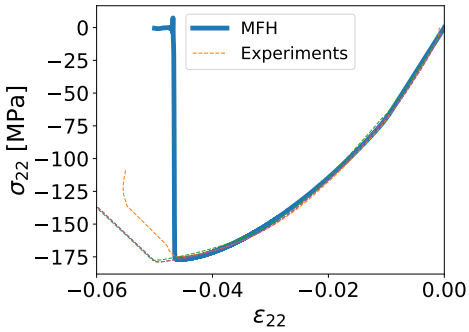

FIGURE 26 MFH multi-scale and experimental stress-strain curves: Experimental tests at $\dot{\varepsilon} = 10^{-4}s^{-1}$ taken from [71].

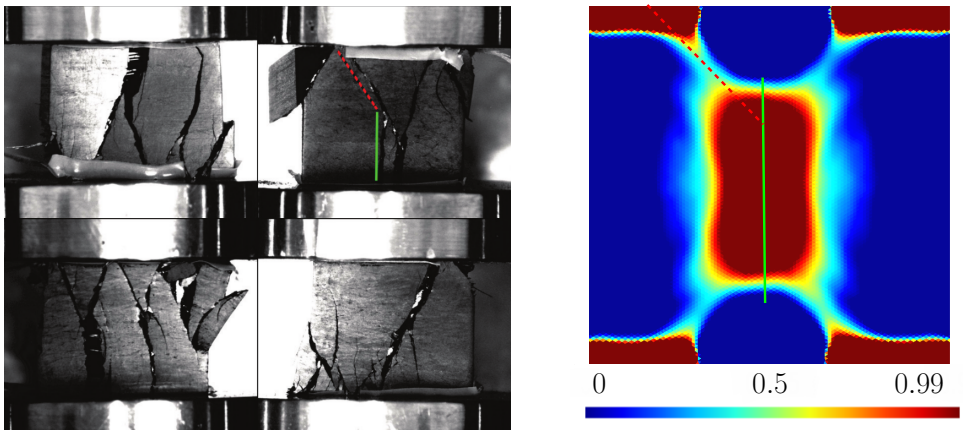

FIGURE 27 Surfaces of the cubic UD specimens after failure as shown in [71] on the left: the green and red lines emphasize the transition between a tensile stress dominated crack propagation to a shear one. Damage [-] contour plot on the deformed sample with a displacement factor of 10 predicted by the multi-scale MFH simulations on the right.

The failure mode observed experimentally is compared to the numerical predictions in Fig. 27. As it can be seen, similar failure patterns can be observed between both results, in which two distinctive fracture directions are found due to the transition from a tensile stress to a shear one.

7 | CONCLUSIONS

In this paper, the incremental-secant MFH process developed by Wu et al. [47,48] was extended by framing a pressure-dependent yield criterion in an incremental-secant formulation. This yield criterion allows capturing the behavior of pressure-sensitive materials such as some epoxy resins while retaining the advantages of using an incremental-secant approach.

It was proved how the isotropic nature of the secant tensors defining the Linear-Comparison-Composite is preserved for the case of a non-associated pressure-dependent plastic flow. This finding is of crucial importance, as it avoids the isotropization step found in most approaches and allows for accurate MFH predictions. This implementation was completed with the possibility to account for damage by using an implicit non-local damage approach, avoiding the loss of ellipticity that is found in local formulations.

This paper has shown the accurate prediction capabilities of the implemented pressure-sensitive residual incremental-secant MFH model in the 2D and 3D cases when considering pure elasto-plasticity and in the damage-enhanced case. Slight discrepancies in the slope of the stress evolution between unloading/compression stages were found in the simulations. The Mori-Tanaka assumption is the principal cause of this phenomenon, with the higher the volume fraction, the higher the discrepancy between the full-field simulation and the MFH prediction. Another cause to this discrepancy is caused by the difference in the matrix material model implementation: although small macro-scale deformation simulations were performed, in the direct simulations

the matrix phase can show large deformations locally when two inclusions are close to each other, and therefore resulting in local large deformation.

In future works, this MFH model will be used to construct a Mean-Field Stochastic Reduced Order Model (MF-ROM)[82], which will allow to perform macro-scale simulations of composites with pressure-dependent matrix materials accounting for the inherent stochastic properties caused by geometrical perturbations in the micro-structure.

8 | ACKNOWLEDGMENTS

The authors would like to acknowledge the financial support from F.R.S.-F.N.R.S.as this publication benefits from the support of the Walloon Region within the framework of a FRIA grant. The authors would also like to acknowledge the supercomputing facilities of the Consortium des Équipements de Calcul Intensif en Federation Wallonie Bruxelles (CÉCI) that were funded by the FRS-FNRS that were made available to us.

□

APPENDIX

A ALGORITHMIC OPERATORS

For the sake of conciseness, in this section the subscript referring to the phase is omitted.

A.1 Residual incremental-secant case

The operator $\boldsymbol{C}^{\text{alg}}$ is defined as:

$$\boldsymbol{C}^{\text{alg}} = \frac{\partial \boldsymbol{\sigma}}{\partial \Delta \boldsymbol{\varepsilon}} = \frac{\partial}{\partial \Delta \boldsymbol{\varepsilon}^{\text{r}}} \left[\Delta \boldsymbol{\sigma}^{\text{r}}\right] : \frac{\partial \Delta \boldsymbol{\varepsilon}^{\text{r}}}{\partial \Delta \boldsymbol{\varepsilon}} = \frac{\partial \Delta \boldsymbol{\sigma}^{\text{r}}}{\partial \Delta \boldsymbol{\varepsilon}^{\text{r}}}. \tag{A1}$$

The term $\frac{\partial}{\partial \Delta \boldsymbol{\varepsilon}^{\text{r}}} \left[\Delta \boldsymbol{\sigma}^{\text{r}}\right]$ can be obtained from Eq. (54), yielding:

$$\begin{aligned} \frac{\partial}{\partial \Delta \boldsymbol{\varepsilon}^{\text{r}}} \left[\Delta \boldsymbol{\sigma}^{\text{r}}\right] = \boldsymbol{C}^{\text{el}} - 6\mu^{\text{el}} \left[\left(\boldsymbol{\sigma}_{n+1}^{\text{tr}} - \boldsymbol{\sigma}_{n}^{\text{res}}\right)^{\text{dev}} \otimes \left(\frac{\left(1 + 6\mu^{\text{el}}\Gamma\right) \frac{\partial \Gamma}{\partial \Delta \boldsymbol{\varepsilon}^{\text{r}}} - 6\mu^{\text{el}}\Gamma \frac{\partial \Gamma}{\partial \Delta \boldsymbol{\varepsilon}^{\text{r}}}}{\left(1 + 6\mu^{\text{el}}\Gamma\right)^2} \right) + \frac{\Gamma}{1 + 6\mu^{\text{el}}\Gamma} \left(2\mu^{\text{el}} \boldsymbol{I}^{\text{dev}}\right) \right] \\ - 2\kappa^{\text{el}}\beta \left[\left(\boldsymbol{\sigma}_{n+1}^{\text{tr}} - \boldsymbol{\sigma}_{n}^{\text{res}}\right)^{\text{vol}} \otimes \left(\frac{\left(1 + 2\kappa^{\text{el}}\beta\Gamma\right) \frac{\partial \Gamma}{\partial \Delta \boldsymbol{\varepsilon}^{\text{r}}} - 2\kappa^{\text{el}}\beta\Gamma \frac{\partial \Gamma}{\partial \Delta \boldsymbol{\varepsilon}^{\text{r}}}}{\left(1 + 2\kappa^{\text{el}}\beta\Gamma\right)^2} \right) + \frac{\Gamma}{1 + 2\beta\kappa^{\text{el}}\Gamma} \left(3\kappa^{\text{el}} \boldsymbol{I}^{\text{vol}}\right) \right], \end{aligned} \tag{A2}$$

where $\frac{\partial \Gamma}{\partial \Delta \boldsymbol{\varepsilon}^{\text{r}}} = \frac{\partial \Gamma}{\partial \Delta \boldsymbol{\varepsilon}}$ is obtained from Eq. (42) from which one can write:

$$0 = \delta f = \left(\frac{\partial f}{\partial \Delta \boldsymbol{\varepsilon}} + \frac{df}{d\Gamma} \frac{\partial \Gamma}{\partial \Delta \boldsymbol{\varepsilon}} \right) : \delta \Delta \boldsymbol{\varepsilon}, \tag{A3}$$

yielding:

$$\frac{\partial \Gamma}{\partial \Delta \boldsymbol{\varepsilon}} = -\left(\frac{df}{d\Gamma} \right)^{-1} \frac{\partial f}{\partial \Delta \boldsymbol{\varepsilon}}. \tag{A4}$$

The term $\frac{df}{d\Gamma}$ comes from the return mapping, Eq. (43), and the term $\frac{\partial f}{\partial \Delta \boldsymbol{\varepsilon}}$ reads

$$\frac{\partial f}{\partial \Delta \boldsymbol{\varepsilon}} = \frac{1}{\boldsymbol{\sigma}_c^{\alpha}} \underbrace{\frac{\partial \left[\left(\frac{\boldsymbol{\sigma}_{n+1}^{\text{tr}} - \boldsymbol{\sigma}_{n}^{\text{res}}}{1 + 6\mu^{\text{el}}\Gamma} + \boldsymbol{\sigma}_{n}^{\text{res}} \right)^{\text{eq}} \right]^{\alpha}}{\partial \Delta \boldsymbol{\varepsilon}}}_{\mathbf{1}*} - 3 \frac{m^{\alpha} - 1}{(m+1)\,\boldsymbol{\sigma}_c} \underbrace{\frac{\partial \left(\frac{\phi_{n+1}^{\text{tr}} - \phi_{n}^{\text{res}}}{1 + 2\kappa^{\text{el}}\Gamma\beta} + \phi_{n}^{\text{res}} \right)}{\partial \Delta \boldsymbol{\varepsilon}}}_{\mathbf{2}*}, \tag{A5}$$

where

$$\mathbf{1} *= \alpha \left[\left(\frac{\boldsymbol{\sigma}_{n+1}^{\mathrm{tr}} - \boldsymbol{\sigma}_{n}^{\mathrm{res}}}{1+6\mu^{\mathrm{el}}\Gamma} + \boldsymbol{\sigma}_{n}^{\mathrm{res}} \right)^{\mathrm{eq}} \right]^{\alpha-1} \frac{\frac{3}{2}\left[\frac{\boldsymbol{I}^{\mathrm{dev}} : \boldsymbol{C}^{\mathrm{el}}}{1+6\mu^{\mathrm{el}}\Gamma} : \left(\frac{\boldsymbol{\sigma}_{n+1}^{\mathrm{tr}} - \boldsymbol{\sigma}_{n}^{\mathrm{res}}}{1+6\mu^{\mathrm{el}}\Gamma} + \boldsymbol{\sigma}_{n}^{\mathrm{res}} \right)^{\mathrm{dev}} \right]}{\sqrt{\frac{3}{2}\left(\frac{\boldsymbol{\sigma}_{n+1}^{\mathrm{tr}} - \boldsymbol{\sigma}_{n}^{\mathrm{res}}}{1+6\mu^{\mathrm{el}}\Gamma} + \boldsymbol{\sigma}_{n}^{\mathrm{res}} \right)^{\mathrm{dev}} : \left(\frac{\boldsymbol{\sigma}_{n+1}^{\mathrm{tr}} - \boldsymbol{\sigma}_{n}^{\mathrm{res}}}{1+6\mu^{\mathrm{el}}\Gamma} + \boldsymbol{\sigma}_{n}^{\mathrm{res}} \right)^{\mathrm{dev}}}}; \qquad \mathbf{2} *= \frac{\kappa^{\mathrm{el}}\mathbf{1}}{1+2\kappa^{\mathrm{el}}\Gamma\beta}. \tag{A6}$$

Finally, one has directly $\boldsymbol{C}_p = \frac{\partial p}{\partial \tilde{p}} = 0$.

A.2 Zero incremental-secant case

In the zero incremental-secant case, the residual stress is not taken into account. The term $\frac{\partial}{\partial \Delta\boldsymbol{\varepsilon}^r}\left[\Delta\boldsymbol{\sigma}^r\right]$ is thus written:

$$\begin{aligned} \frac{\partial}{\partial \Delta\boldsymbol{\varepsilon}^r}\left[\Delta\sigma^r\right] =& \boldsymbol{C}^{\mathrm{el}} - 6\mu^{\mathrm{el}}\left[\left(\boldsymbol{\sigma}_{n+1}^{\mathrm{tr}}\right)^{\mathrm{dev}} \otimes \left(\frac{\left(1+6\mu^{\mathrm{el}}\Gamma\right)\frac{\partial\Gamma}{\partial\Delta\boldsymbol{\varepsilon}^r} - 6\mu^{\mathrm{el}}\Gamma\frac{\partial\Gamma}{\partial\Delta\boldsymbol{\varepsilon}^r}}{\left(1+6\mu^{\mathrm{el}}\Gamma\right)^2} \right) + \frac{\Gamma}{1+6\mu^{\mathrm{el}}\Gamma}\left(2\mu^{\mathrm{el}}\boldsymbol{I}^{\mathrm{dev}}\right) \right] \\ & - 2\kappa^{\mathrm{el}}\beta\left[\left(\boldsymbol{\sigma}_{n+1}^{\mathrm{tr}}\right)^{\mathrm{vol}} \otimes \left(\frac{\left(1+2\kappa^{\mathrm{el}}\beta\Gamma\right)\frac{\partial\Gamma}{\partial\Delta\boldsymbol{\varepsilon}^r} - 2\kappa^{\mathrm{el}}\beta\Gamma\frac{\partial\Gamma}{\partial\Delta\boldsymbol{\varepsilon}^r}}{\left(1+2\kappa^{\mathrm{el}}\beta\Gamma\right)^2} \right) + \frac{\Gamma}{1+2\beta\kappa^{\mathrm{el}}\Gamma}\left(3\kappa^{\mathrm{el}}\boldsymbol{I}^{\mathrm{vol}}\right) \right], \end{aligned} \tag{A7}$$

where the terms defining $\frac{\partial\Gamma}{\partial\Delta\varepsilon^{\mathrm{r}}} = \frac{\partial\Gamma}{\partial\Delta\boldsymbol{\varepsilon}} = -\left(\frac{df}{d\Gamma}\right)^{-1}\frac{\partial f}{\partial\Delta\boldsymbol{\varepsilon}}$ read

$$\frac{\partial f}{\partial\Delta\boldsymbol{\varepsilon}} = \frac{1}{\sigma_c^{\alpha}} \underbrace{\frac{\partial\left[\left(\frac{\boldsymbol{\sigma}_{n+1}^{\mathrm{tr}}}{1+6\mu^{\mathrm{el}}\Gamma}\right)^{\mathrm{eq}}\right]^{\alpha}}{\partial\Delta\boldsymbol{\varepsilon}}}_{\mathbf{1}*} - 3\frac{m^{\alpha}-1}{(m+1)\,\sigma_c} \underbrace{\frac{\partial\left(\frac{\phi_{n+1}^{\mathrm{tr}}}{1+2\kappa^{\mathrm{el}}\Gamma\beta}\right)}{\partial\Delta\boldsymbol{\varepsilon}}}_{\mathbf{2}*}, \tag{A8}$$

with

$$\mathbf{1} *= \alpha \left[\left(\frac{\boldsymbol{\sigma}_{n+1}^{\mathrm{tr}}}{1+6\mu^{\mathrm{el}}\Gamma} \right)^{\mathrm{eq}} \right]^{\alpha-1} \frac{\frac{3}{2}\left[\frac{\boldsymbol{I}^{\mathrm{dev}} : \boldsymbol{C}^{\mathrm{el}}}{1+6\mu^{\mathrm{el}}\Gamma} : \left(\frac{\boldsymbol{\sigma}_{n+1}^{\mathrm{tr}}}{1+6\mu^{\mathrm{el}}\Gamma} \right)^{\mathrm{dev}} \right]}{\sqrt{\frac{3}{2}\left(\frac{\boldsymbol{\sigma}_{n+1}^{\mathrm{tr}}}{1+6\mu^{\mathrm{el}}\Gamma} \right)^{\mathrm{dev}} : \left(\frac{\boldsymbol{\sigma}_{n+1}^{\mathrm{tr}}}{1+6\mu^{\mathrm{el}}\Gamma} \right)^{\mathrm{dev}}}}, \qquad \mathbf{2} *= \frac{\kappa^{\mathrm{el}}\mathbf{1}}{1+2\kappa^{\mathrm{el}}\Gamma\beta}; \tag{A9}$$

and

$$\frac{df}{d\Gamma} = \left[-\frac{\alpha}{\sigma_c^{\alpha+1}}\frac{\partial R(\Delta p)}{\partial \Delta p}\left(\left(\frac{\hat{\boldsymbol{\sigma}}_{n+1}^{\mathrm{tr}}}{1+6\mu^{\mathrm{el}}\Gamma} \right)^{\mathrm{eq}} \right)^{\alpha} + 3\frac{m^{\alpha}-1}{(m+1)\sigma_c^2}\frac{\partial R(\Delta p)}{\partial \Delta p}\left(\frac{\hat{\phi}_{n+1}^{\mathrm{tr}}}{1+2\kappa^{\mathrm{el}}\Gamma\beta} \right) \right]\frac{\partial\Delta p}{\partial\Gamma} + \frac{\partial f}{\partial\Gamma}; \tag{A10}$$

$$\frac{\partial f}{\partial\Gamma} = -\alpha\left(\frac{\left(\frac{\hat{\boldsymbol{\sigma}}_{n+1}^{\mathrm{tr}}}{1+6\mu^{\mathrm{el}}\Gamma}\right)^{\mathrm{eq}}}{\sigma_c} \right)^{\alpha-1} \frac{9\mu^{\mathrm{el}}\left(\hat{\boldsymbol{\sigma}}_{n+1}^{\mathrm{tr}}\right)^{\mathrm{dev}} : \left(\frac{\hat{\boldsymbol{\sigma}}_{n+1}^{\mathrm{tr}}}{1+6\mu^{\mathrm{el}}\Gamma}\right)^{\mathrm{dev}}}{\sigma_c\left(1+6\mu^{\mathrm{el}}\Gamma\right)^2\left(\frac{\hat{\boldsymbol{\sigma}}_{n+1}^{\mathrm{tr}}}{1+6\mu^{\mathrm{el}}\Gamma}\right)^{\mathrm{eq}}} + 3\frac{m^{\alpha}-1}{(m+1)\,\sigma_c}\left(\frac{\hat{\phi}_{n+1}^{\mathrm{tr}}}{\left(1+2\kappa^{\mathrm{el}}\Gamma\beta\right)^2}2\kappa^{\mathrm{el}}\beta \right). \tag{A11}$$

Finally, one has directly $\boldsymbol{C}_p = \frac{\partial p}{\partial \tilde{p}} = 0$.

B STRESS RESIDUAL VECTOR

In this section, $\boldsymbol{C}^{\mathrm{S}}$, κ_s, μ_s and $\boldsymbol{C}^{\mathrm{SD}}$, κ_s^{D} and μ_s^{D} respectively stand either for $\boldsymbol{C}^{\mathrm{Sr}}$, Eq. (56), κ_s^{r}, μ_s^{r}, Eq. (57), $\boldsymbol{C}^{\mathrm{SDr}}$, Eq. (61), κ_s^{Dr} and μ_s^{Dr}, Eq. (63), or for $\boldsymbol{C}^{\mathrm{S0}}$, Eq. (59), κ_s^0, μ_s^0, Eq. (60), $\boldsymbol{C}^{\mathrm{SD0}}$, Eq. (64), κ_s^{D0} and μ_s^{D0}, Eq. (66).

At the end of the MFH scheme we must satisfy:

$$\Delta\boldsymbol{\varepsilon}_{\mathrm{I}n+1}^{\mathrm{r}} = \boldsymbol{B}^{\epsilon}\left(\mathrm{I}, \boldsymbol{C}_0^{\mathrm{SD}}, \boldsymbol{C}_{\mathrm{I}}^{\mathrm{S}}\right) : \Delta\boldsymbol{\varepsilon}_{0n+1}^{\mathrm{r}}. \tag{B12}$$

For a two-phase composite, the relation of the variation of strains in the full composite and each of its phases writes

$$\Delta\bar{\boldsymbol{\varepsilon}}^{\mathrm{r}}_{n+1} = v_0\Delta\boldsymbol{\varepsilon}^{\mathrm{r}}_{0n+1} + v_{\mathrm{I}}\Delta\boldsymbol{\varepsilon}^{\mathrm{r}}_{\mathrm{I}n+1}. \tag{B13}$$

Multiplying Eq. (B13) by the concentration strain tensor and using Eq. (B12), one has

$$v_0\Delta\boldsymbol{\varepsilon}^{\mathrm{r}}_{\mathrm{I}n+1} + v_{\mathrm{I}}\boldsymbol{B}^{\epsilon}\left(\mathrm{I}, \boldsymbol{C}^{\mathrm{SD}}_0, \boldsymbol{C}^{\mathrm{S}}_{\mathrm{I}}\right) : \Delta\boldsymbol{\varepsilon}^{\mathrm{r}}_{\mathrm{I}n+1} = \boldsymbol{B}^{\epsilon}\left(\mathrm{I}, \boldsymbol{C}^{\mathrm{SD}}_0, \boldsymbol{C}^{\mathrm{S}}_{\mathrm{I}}\right) : \Delta\bar{\boldsymbol{\varepsilon}}^{\mathrm{r}}_{n+1}. \tag{B14}$$

Using Mori-Tanaka assumption (5) for $\boldsymbol{B}^{\epsilon}$, Eq. (B14) is rewritten

$$\Delta\boldsymbol{\varepsilon}^{\mathrm{r}}_{\mathrm{I}n+1} + v_0\boldsymbol{S} : \left[\left(\boldsymbol{C}^{\mathrm{SD}}_0\right)^{-1} : \boldsymbol{C}^{\mathrm{S}}_{\mathrm{I}} - \boldsymbol{I}\right] : \Delta\boldsymbol{\varepsilon}^{\mathrm{r}}_{\mathrm{I}_{n+1}} = \Delta\bar{\boldsymbol{\varepsilon}}^{\mathrm{r}}_{n+1}\,. \tag{B15}$$

It is then possible to write the stress residual vector $\boldsymbol{F} = 0$ as

$$\boldsymbol{F} = \boldsymbol{C}^{\mathrm{SD}}_0 : \left[\Delta\boldsymbol{\varepsilon}^{\mathrm{r}}_{\mathrm{I}n+1} - \frac{1}{v_0}\boldsymbol{S}^{-1} : \left(\Delta\boldsymbol{\varepsilon}^{\mathrm{r}}_{\mathrm{I}n+1} - \Delta\bar{\boldsymbol{\varepsilon}}^{\mathrm{r}}_{n+1}\right)\right] - \boldsymbol{C}^{\mathrm{S}}_{\mathrm{I}} : \Delta\boldsymbol{\varepsilon}^{\mathrm{r}}_{\mathrm{I}n+1}. \tag{B16}$$

This residual can be linearized as

$$\mathrm{d}\boldsymbol{F} = \frac{\partial\boldsymbol{F}}{\partial\boldsymbol{\varepsilon}_{\mathrm{I}}} : \mathrm{d}\Delta\boldsymbol{\varepsilon}^{\mathrm{r}}_{\mathrm{I}} + \frac{\partial\boldsymbol{F}}{\partial\boldsymbol{\varepsilon}_0} : \mathrm{d}\Delta\boldsymbol{\varepsilon}^{\mathrm{r}}_0 + \frac{\partial\boldsymbol{F}}{\partial\bar{\boldsymbol{\varepsilon}}} : \mathrm{d}\Delta\bar{\boldsymbol{\varepsilon}}^{\mathrm{r}} + \frac{\partial\boldsymbol{F}}{\partial\tilde{p}_0}\,\mathrm{d}\tilde{p}_0. \tag{B17}$$

In order to solve $\boldsymbol{F} = 0$, we consider constant $\Delta\bar{\boldsymbol{\varepsilon}}^{\mathrm{r}}$ and $\tilde{p}_0$ values. The process therefore yields $\mathrm{d}\boldsymbol{F} = \boldsymbol{J} : \mathrm{d}\boldsymbol{\varepsilon}_{\mathrm{I}}$, where $\boldsymbol{J}$ writes:

$$\begin{aligned}
\boldsymbol{J} =& \frac{\partial\boldsymbol{F}}{\partial\boldsymbol{\varepsilon}_{\mathrm{I}}} + \frac{\partial\boldsymbol{F}}{\partial\boldsymbol{\varepsilon}_0} : \frac{\partial\boldsymbol{\varepsilon}_0}{\partial\boldsymbol{\varepsilon}_{\mathrm{I}}} \\
=& \boldsymbol{C}^{\mathrm{SD}}_{0\,n+1} : \left[\boldsymbol{I} - \boldsymbol{S}^{-1}\right] - \boldsymbol{C}^{\mathrm{S}}_{\mathrm{I}_{n+1}} - \frac{\partial\boldsymbol{C}^{\mathrm{S}}_{\mathrm{I}n+1}}{\partial\boldsymbol{\varepsilon}_{\mathrm{I}}} : \Delta\boldsymbol{\varepsilon}^{\mathrm{r}}_{\mathrm{I}n+1} - \\
& \frac{v_{\mathrm{I}}}{v_0}\left(\frac{\partial\boldsymbol{C}^{\mathrm{SD}}_{0\,n+1}}{\partial\boldsymbol{\varepsilon}_0} + \frac{\partial\boldsymbol{C}^{\mathrm{SD}}_{0\,n+1}}{\partial\boldsymbol{D}_0}\frac{\partial\boldsymbol{D}_0}{\partial\boldsymbol{\varepsilon}_0}\right) : \left[\Delta\boldsymbol{\varepsilon}^{\mathrm{r}}_{\mathrm{I}n+1} - \boldsymbol{S}^{-1} : \frac{\left(\Delta\boldsymbol{\varepsilon}^{\mathrm{r}}_{\mathrm{I}n+1} - \Delta\bar{\boldsymbol{\varepsilon}}^{\mathrm{r}}_{n+1}\right)}{v_0}\right] - \\
& \frac{v_{\mathrm{I}}}{v_0^2}\boldsymbol{C}^{\mathrm{SD}}_{0\,n+1} \otimes \left(\Delta\boldsymbol{\varepsilon}^{\mathrm{r}}_{\mathrm{I}n+1} - \Delta\bar{\boldsymbol{\varepsilon}}^{\mathrm{r}}_{n+1}\right) :: \left(\boldsymbol{S}^{-1} \otimes \boldsymbol{S}^{-1}\right) :: \left(\frac{\partial\boldsymbol{S}}{\partial\boldsymbol{\varepsilon}_0} + \frac{\partial\boldsymbol{S}}{\partial\boldsymbol{D}_0}\frac{\partial\boldsymbol{D}_0}{\partial\boldsymbol{\varepsilon}_0}\right) - \frac{v_{\mathrm{I}}}{v_0}\boldsymbol{C}^{\mathrm{SD}}_{0\,n+1} : \boldsymbol{S}^{-1},
\end{aligned} \tag{B18}$$

where the derivative of the Eshelby tensor is given in Appendix D.

Then, the strain increment in each phase due to the variation $\mathrm{d}\Delta\bar{\boldsymbol{\varepsilon}}^{\mathrm{r}}$ is computed by constraining $d\boldsymbol{F} = 0$, being possible to write

$$\frac{\partial\boldsymbol{\varepsilon}_{\mathrm{I}}}{\partial\bar{\boldsymbol{\varepsilon}}} = -\boldsymbol{J}^{-1} : \frac{\partial\boldsymbol{F}}{\partial\bar{\boldsymbol{\varepsilon}}}\,,\ \text{and}\ \frac{\partial\boldsymbol{\varepsilon}_{\mathrm{I}}}{\partial\tilde{p}_0} = -\boldsymbol{J}^{-1} : \frac{\partial\boldsymbol{F}}{\partial\tilde{p}_0}\,. \tag{B19}$$

The set of equations is completed with the use of the relation between the strains increments $\mathrm{d}\bar{\boldsymbol{\varepsilon}}^{\mathrm{r}} = v_0\mathrm{d}\boldsymbol{\varepsilon}^{\mathrm{r}}_0 + v_{\mathrm{I}}\mathrm{d}\boldsymbol{\varepsilon}^{\mathrm{r}}_{\mathrm{I}}$, yielding

$$\frac{\partial\boldsymbol{\varepsilon}_0}{\partial\bar{\boldsymbol{\varepsilon}}} = \frac{1}{v_0}\left(\boldsymbol{I} - v_1\frac{\partial\boldsymbol{\varepsilon}_{\mathrm{I}}}{\partial\bar{\boldsymbol{\varepsilon}}}\right)\,,\ \text{and}\ \frac{\partial\boldsymbol{\varepsilon}_0}{\partial\tilde{p}_0} = -\frac{v_{\mathrm{I}}}{v_0}\frac{\partial\boldsymbol{\varepsilon}_{\mathrm{I}}}{\partial\tilde{p}_0}. \tag{B20}$$

Appendix C details the derivative of $\boldsymbol{C}^{\mathrm{Sr}}$ and $\boldsymbol{C}^{\mathrm{S0}}$ with respect to $\boldsymbol{\varepsilon}$, which completes the process.

C DERIVATIVES OF SECANT OPERATORS

For the sake of conciseness, in this section the subscript referring to the phase is omitted. Besides, $\boldsymbol{C}^{\mathrm{S}}$, κ_s, μ_s and $\boldsymbol{C}^{\mathrm{SD}}$, κ_s^{D} and μ_s^{D} respectively stand either for $\boldsymbol{C}^{\mathrm{Sr}}$, Eq. (56), κ_s^{r}, μ_s^{r}, Eq. (57), $\boldsymbol{C}^{\mathrm{SDr}}$, Eq. (61), κ_s^{Dr} and μ_s^{Dr}, Eq. (63), or for $\boldsymbol{C}^{\mathrm{S0}}$, Eq. (59), κ_s^{0}, μ_s^{0}, Eq. (60), $\boldsymbol{C}^{\mathrm{SD0}}$, Eq. (64), κ_s^{D0} and μ_s^{D0}, Eq. (66).

The derivative of $\boldsymbol{C}^{\mathrm{S}}$ writes

$$\frac{\partial\boldsymbol{C}^{\mathrm{S}}}{\partial\boldsymbol{\varepsilon}} = \frac{\partial}{\partial\Delta\boldsymbol{\varepsilon}^{\mathrm{r}}}\left(3\kappa_s\boldsymbol{I}^{\mathrm{vol}} + 2\mu_s\boldsymbol{I}^{\mathrm{dev}}\right) : \frac{\partial\Delta\boldsymbol{\varepsilon}^{\mathrm{r}}}{\partial\boldsymbol{\varepsilon}} = \left(3\boldsymbol{I}^{\mathrm{vol}}\frac{\partial\kappa_s}{\partial\Gamma} + 2\boldsymbol{I}^{\mathrm{dev}}\frac{\partial\mu_s}{\partial\Gamma}\right) \otimes \frac{\partial\Gamma}{\partial\boldsymbol{\varepsilon}}, \tag{C21}$$

where the derivative $\frac{\partial\Gamma}{\partial\boldsymbol{\varepsilon}}$ is given in appendix A and the derivatives of the bulk and shear moduli read

$$\frac{\partial\mu_s}{\partial\Gamma} = -\frac{6{\mu^{\mathrm{el}}}^2}{\left(1 + 6\mu^{\mathrm{el}}\Gamma\right)^2},\ \text{and}\ \frac{\partial\kappa_s}{\partial\Gamma} = -\frac{2\beta{\kappa^{\mathrm{el}}}^2}{\left(1 + 2\kappa^{\mathrm{el}}\Gamma\beta\right)^2}. \tag{C22}$$

In the damaged enhanced case, the derivative of the damaged secant tensors become

$$\frac{\mathrm{d}\boldsymbol{C}^{\mathrm{SD}}}{\mathrm{d}\boldsymbol{\varepsilon}} = \frac{\partial \boldsymbol{C}^{\mathrm{SD}}}{\partial \boldsymbol{\varepsilon}} + \frac{\partial \boldsymbol{C}^{\mathrm{SD}}}{\partial D}\frac{\partial D}{\partial \boldsymbol{\varepsilon}} = (1-D)\frac{\partial \boldsymbol{C}^{\mathrm{S}}}{\partial \boldsymbol{\varepsilon}} - \boldsymbol{C}^{\mathrm{S}} \otimes \frac{\partial D}{\partial \boldsymbol{\varepsilon}}, \tag{C23}$$

where the derivative $\frac{\partial D}{\partial \boldsymbol{\varepsilon}}$ is given in Appendix E.

D ESHELBY TENSOR DERIVATIVES

For the sake of conciseness, in this section the subscript referring to the phase is omitted. Besides, $\boldsymbol{C}^{\mathrm{S}}$, κ_s, μ_s and $\boldsymbol{C}^{\mathrm{SD}}$, κ_s^{D} and μ_s^{D} respectively stand either for $\boldsymbol{C}^{\mathrm{Sr}}$, Eq. (56), κ_s^{r}, μ_s^{r}, Eq. (57), $\boldsymbol{C}^{\mathrm{SDr}}$, Eq. (61), κ_s^{Dr} and μ_s^{Dr}, Eq. (63), or for $\boldsymbol{C}^{\mathrm{S0}}$, Eq. (59), κ_s^{0}, μ_s^{0}, Eq. (60), $\boldsymbol{C}^{\mathrm{SD0}}$, Eq. (64), κ_s^{D0} and μ_s^{D0}, Eq. (66).

For the elasto-plastic case, the derivative of the Eshelby tensor writes:

$$\frac{\partial \boldsymbol{S}}{\partial \Delta\boldsymbol{\varepsilon}^{\mathrm{r}}} = \frac{\partial \boldsymbol{S}}{\partial \nu} \otimes \left(\frac{\partial \nu}{\partial \kappa_s}\frac{\partial \kappa_s}{\partial \Gamma} + \frac{\partial \nu}{\partial \mu_s}\frac{\partial \mu_s}{\partial \Gamma} \right) \frac{\partial \Gamma}{\partial \Delta\boldsymbol{\varepsilon}^{\mathrm{r}}}, \tag{D24}$$

where the derivative $\frac{\partial \Gamma}{\partial \boldsymbol{\varepsilon}}$ is given in appendix A and the derivatives of the bulk and shear moduli are given in Eq. (C22).

For the damage-enhanced elasto-plastic case, in which the damaged secant moduli are used, the derivative of the Eshelby tensor is written as

$$\frac{\partial \boldsymbol{S}}{\partial \Delta\boldsymbol{\varepsilon}^{\mathrm{r}}} = \frac{\partial \boldsymbol{S}}{\partial \nu} \otimes \left[\frac{\partial \nu}{\partial \kappa_s^D} \left(-\frac{\partial D}{\partial \boldsymbol{\varepsilon}^{\mathrm{r}}}\kappa_s + (1-D)\frac{\partial \kappa_s}{\partial \Gamma}\frac{\partial \Gamma}{\partial \Delta\boldsymbol{\varepsilon}^{\mathrm{r}}} \right) + \frac{\partial \nu}{\partial \mu_s^D} \left(-\frac{\partial D}{\partial \boldsymbol{\varepsilon}^{\mathrm{r}}}\mu_s + (1-D)\frac{\partial \mu_s}{\partial \Gamma}\frac{\partial \Gamma}{\partial \Delta\boldsymbol{\varepsilon}^{\mathrm{r}}} \right) \right], \tag{D25}$$

where $\frac{\partial D}{\partial \boldsymbol{\varepsilon}^{\mathrm{r}}}$ is given in Appendix E.

E DERIVATIVES OF THE DAMAGE LAW

For the sake of conciseness, in this section the subscript referring to the phase is omitted.

By using the damage evolution law depicted in Eq. (87), the derivatives needed for the incremental-secant based MFH implementation write

$$\frac{\partial D}{\partial \boldsymbol{\varepsilon}} = \frac{\partial D}{\partial \Delta\boldsymbol{\varepsilon}^{\mathrm{r}}} = 0, \tag{E26}$$

and

$$\frac{\partial D}{\partial \tilde{p}} = \begin{cases} \frac{\widetilde{D}_{onset}}{\widetilde{p}_{onset}}, & \text{if} \quad \tilde{p}_0 \leq \tilde{p}_{onset}\,; \\ \frac{\widetilde{D}_{onset}}{\widetilde{p}_{onset}} + \alpha\beta\left(\widetilde{p}_0 + \Delta\widetilde{p}_0 - \widetilde{p}_{\mathrm{onset}}\right)^{\beta-1}\Delta\widetilde{p}_0 + \alpha\left(\widetilde{p}_0 + \Delta\widetilde{p}_0 - \widetilde{p}_{\mathrm{onset}}\right)^{\beta} & \text{if} \quad \tilde{p}_0 > \tilde{p}_{onset}\,. \end{cases} \tag{E27}$$

F DAMAGE-ENHANCED 2D TESTS

Uniaxial, shear and biaxial loading

Concerning the uniaxial cycle test, looking at Fig. F1 the same comments as on the elasto-plastic case can be applied to this simulation since an overestimation of the stress seen by the material on the final stage of the loading path. As shown in Fig. F1, similar results are obtained again for the low strain shear cyclic loading, proving once again that the presence of damage in the matrix has no impact in the MFH prediction capabilities. A slight difference in slope is seen as in the previous cases in the unloading path, but one can conclude that the damaged matrix case under shear loading is well captured by the MFH scheme.

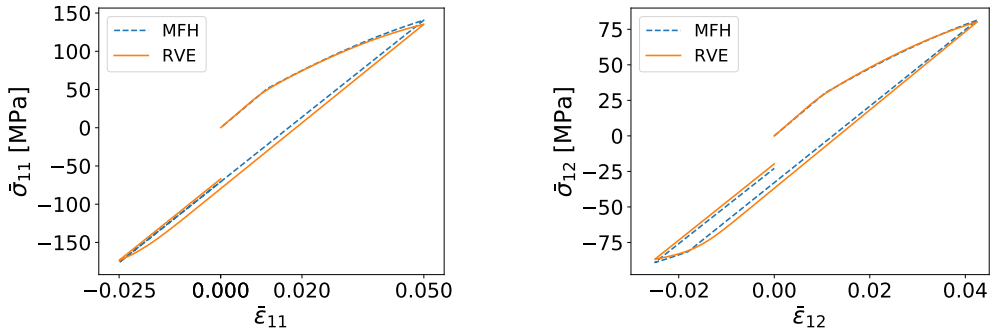

FIGURE F1 Stress-strain curves for the damage-enhanced uniaxial loading test on a 40% 2D UD sample(left), and Stress-strain curves for the damage-enhanced shear loading test on a 40% 2D UD sample (right).

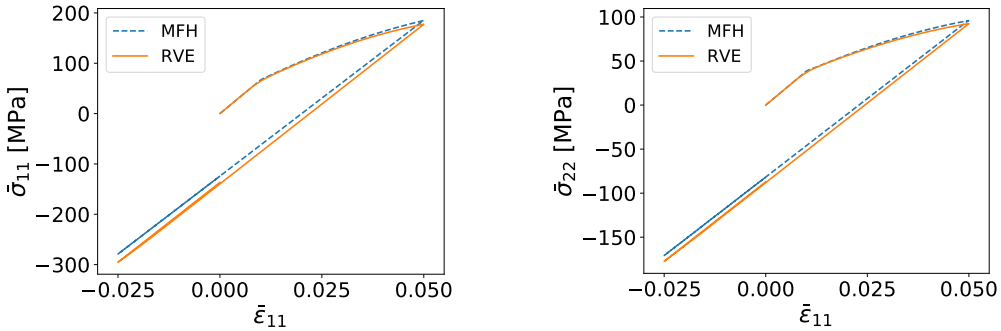

FIGURE F2 Loading and transverse direction stress-strain curves for damage-enhanced biaxial loading test ($\varepsilon_{22} = 0$) on the 40% fiber volume fraction 2D UD RVE sample.

The next test used to compare the MFH performance with the full-field simulation is biaxial tension. This simulation allows assessing how the MFH scheme is able to correctly represent the pressure-dependent behavior in the case where damage is present in the matrix. Fig. F2 proves the accuracy of the MFH simulation is not impacted by the presence of damage in the matrix and it is able to capture correctly the behavior of the composite on both plane directions.

Non-Proportional Loading

The same non-proportional loading test as the one performed for the elasto-plastic case is now performed taking damage into account, so that the impact of damage on the obtained result can be addressed. Figs. F3 and F4 show a good behavior of the MFH prediction under non-proportional loading conditions when damage is taken into account. The first half of the simulation in which the loading occurs, the composite behavior is correctly captured for both tests, where a slightly stiff behavior is encountered, overestimating the stress seeing by the composite. As already discussed, the difference in the slope during the unloading phases of the cycle is still present, however, the obtained MFH prediction can be said to be satisfactory.

References

1. Kanouté P, Boso D, Chaboche J, Schrefler B. Multiscale Methods for Composites: A Review. *Archives of Computational Methods in Engineering* 2009; 16: 31-75.

2. Geers M, Kouznetsova V, Brekeclmans W. Multi-scale computational homogenization: Trends and challenges. *Journal of Comp. and Appl. Math.* 2010; 234: 20175-2182.

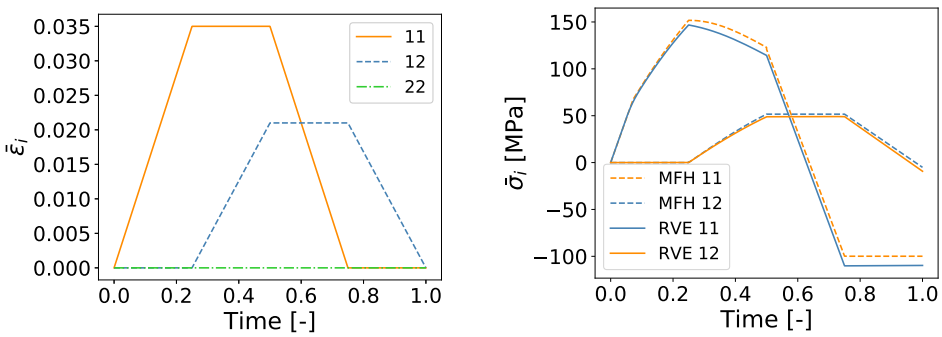

FIGURE F3 Strain-time evolution (left) and stress-time evolution (right) of the damage-enhanced non-proportional loading with zero-transverse strain on a 40% volume fraction 2D UD sample.

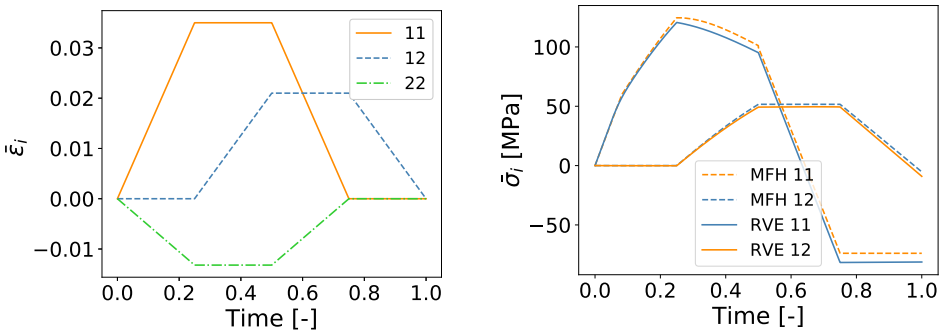

FIGURE F4 Strain-time evolution (left) and stress-time evolution (right) of the damage-enhanced non-proportional loading with transverse compression on a 40% volume fraction 2D UD sample.

3. Llorca J, González C, Molina-Aldareguía J, et al. Multiscale modeling of composite materials: a roadmap towards virtual testing. *Adv. Mat.* 2011; 23: 5130-5147.

4. Nemat-Nasser S, Hori M. Micromechanics: overall properties of heterogeneous materials. 2013; 37.

5. Noels L, Wu L, Adam L. Review of homogenization methods for heterogeneous materials. *Handbook of Software Solutions for ICME* 2016; 6.1.1.: 433-441.

6. Ghosh S, Lee K, Moorthy S. Multiple scale analysis of heterogeneous elastic structures using homogenization theory and voronoi cell finite element method. *International Journal of Solids and Structures* 1995; 32(1): 27-62.

7. Lissenden C, Arnold S. Theoretical and experimental considerations in representing macroscale flow/damage surfaces for metal matrix composites. *Int. J. Plasticity* 1997; 13: 327-358.

8. Wieckowski Z. Dual finite element methods in homogenization for elasticplastic fibrous composite material. *Int. J. Plasticity* 2000; 16: 199-221.

9. Segurado J, Llorca J, González C. On the accuracy of mean field approaches to simulate the plastic deformation of composites. *Scripta Mater* 2002; 46: 525-529.

10. Ju B, Wang T. Plastic constitutive behavior of short-fiber particle reinforced composites. *Int. J. Plasticity* 2003; 19: 565-581.

11. Carrere N, Valle R, Bretheau T, Chaboche J. Multiscale analysis of the transverese properties of ti-based matrix composites reinforced by sic fibres: from the grain scale to the macroscopic scale. *Int. J. Plasticity* 2004; 20: 783-810.

12. Michel J, Moulinec H, Suquet P. Effective properties of composite materials with periodic microstructure: a computational approach. *Computer Methods in Applied Mechanics and Engineering* 1999; 172: 109âĂŞ143.

13. Feyel F. Multiscale FE2 elastoviscoplastic analysis of composite structures. *Computational Materials Science* 1999; 16: 344-354.

14. Terada K, Hori M, Kyoya T, Kikuchi N. Simulation of the multi-scale convergence in computational homogenization approaches. *International Journal of Solids and Structures* 2000; 37: 2285âĂŞ2311.

15. Kouznetsova V, Brekelmans W, Baaijens F. An approach to micro-macro modeling of heterogeneous materials. *Computational Mechanics* 2001; 27(1): 37-48.

16. Kouznetsova V, Geers M, Brekelmans W. Multi-scale second-order computational homogenization of muli-phase materials: a nested finite element solution strategy. *Comput. Methods Appl. Mech. Eng.* 2004; 193: 5525-5550.

17. Eshelby J. The determination of the elastic field of an ellipsoidal inclusion and related problems. *Proceedings of the Royal Society of London. Seres A, Mathematical and Physical Sciences* 1957; 241: 376-396.

18. Kröner E. Berechnung der elastischen konstanten des vielkristalls aus den konstanten des einkistalls. *Z phys. A-Hadron Nucl.* 1958; 151: 504-518.

19. Hill R. Continuum micro-mechanics of elastoplastic polycristals. *J. Mech. Phys. Soldis* 1965a; 13: 89-101.

20. Hill R. A self-consisten mechanics of composite materials. *J. Mech. Phys. Soldis* 1965b; 13: 213-222.

21. Maalej Y, Imene El Ghezal M, Doghri I. Elasticity and viscoelasticity of open cellular material: micromechanical approach. *M. Haddar et al. (Eds.): Design and Modeling of Mechanical Systems* 2013: 531âĂŞ540.

22. Mori T, Tanaka K. Average stress in matrix and average elastic energy of materials with misfitting inclusions. *Acta Metall* 1973; 21: 571-574.

23. Hashin Z. The elastic moduli of heterogeneous materials. *ASME J. Appl. Mech.* 1962; 29: 143-150.

24. Christensen R, Lo K. Solutions for effective shear properties in three phase sphere and cylinder models. *Mech. Phys. Solids* 1979; 27: 315-330.

25. Hori M, Nemat-Nasser S. Double-inclusion model and overall moduli of multi-phase composites. *Mech. of Mech.* 1993; 14: 189-206.

26. Ponte Castañeda P. The effective mechanical properties of nonlinear isotropic composites. *Journal of the Mechanics and Physics of Solids* 1991; 39(1): 45-71.

27. Ponte Castañeda P. A new variational principle and its application to nonlinear heterogeneous systems. *SIAM Journal on Appl. Math.* 1992; 52: 1321-1341.

28. Lahellec N, Suquet P. On the effective behavior of nonlinear inelastic composites: I. incremental variational principles. *Journal of the mech. and Phys. of Solids* 2007a; 55: 1932-1963.

29. Lahellec N, Suquet P. On the effective behavior of nonlinear inelastic composites: II. A second-order procedure. *Journal of the mech. and Phys. of Solids* 2007b; 55: 1964-1992.

30. Miehe C. Strain-driven homogenization of inelastic microstructures and composites based on an incremental variational formulation. *International Journal for Numerical Methods in Engineering* 2002; 55(11): 1285-1322.

31. Brassart L, Stainier L, Doghri I, Delannay L. A variational formulation for the incremental homogenization of elasto-plastic composites. *Journal of the mech. and Phys. of Solids* 2011; 59: 2455 - 2475.

32. Brassart L, Stainier L, Doghri I, Delannay L. Homogenization of elasto-(visco) plastic composites based on an incremental variational principle. *Int. Journal of Plast.* 2012; 36: 86-112.

33. Boudet J, Auslender F, Bornert M, Lapusta Y. An incremental variational formulation for the prediction of the effective work-hardening behavior and field statistics ofelasto-(visco)plastic composites. *International Journal of Solids and Structures* 2016; 83: 90-113.

34. Lucchetta A, Auslender F, Bornert M, Kondo D. A double incremental variational procedure for elastoplastic composites with combined isotropic and linear kinematic hardening. *International Journal of Solids and Structures* 2019; 158: 243-267.

35. Lucchetta A, Auslender F, Bornert M, Kondo D. Incremental variational homogenization of elastoplastic composites with isotropic and Armstrong-Frederick type nonlinear kinematic hardening. *International Journal of Solids and Structures* 2021; 222 - 223.

36. Berveiller M, Zaoui A. An extension of the self-consistent scheme to plastically-flowing polycrystals. *Journal of the Mech. and Phys. of Solids* 1978; 26: 325-344.

37. Tandom G, Weng G. A theory of particle-reinforced plasticity. *Journal of Appl. Mech.* 1988; 55: 126-135.

38. Molinari A, Canova G, Ahzi S. A self consistent approach of the large deformation polycristal viscoplasticity. *Acta Metallurgica* 1987; 35: 2983-2994.

39. Masson R, Borner M, Suquet P, Zaoui A. An affine formulation for the prediction of the effective properties of nonlinear composites and polycrystals. *Journal Mech. Of Phys. Of Solids* 2000; 48: 1203-1227.

40. Pierard O, Doghri I. An enhanced affine formulation and the corresponding numerical algorithms for the mean-field homogenization of elasto-viscoplastic composites. *Int. Journal of Plast.* 2006a; 22: 131-157.

41. Doghri I, Adam L, Bilger N. Mean-field homogenization of elasto-viscoplastic composites based on a general incrementally affine linearization method. *Int. Journal of Plast.* 2010; 26: 219-238.

42. Miled B, Doghri I, Brassart L, Delannay L. Micromechanical modeling of coupled viscoelastic-viscoplastic composites based on an incrementally affine formulation. *Int. Journal of Sol. and Struct.* 2013; 50: 1755-1769.

43. Hutchinson J. Elastic-plastic behaviour of polycrystalline metals and composites. *Proc. of the Roy. Soc. of London. A. Math. and Phys. Sci.* 1970; 319: 247-272.

44. Doghri I, Ouaar A. Homogenization of two-phase elasto-plastic composite materials and structures: Study of tangent operators, cyclic plasticity and numerical algorithms. *Int. Jounal of Solids and Struc.* 2003; 40: 1681-1712.

45. S.Mercier , K.Kowalczyk-Gajewska , C.Czarnota . Effective behavior of composites with combined kinematic and isotropic hardening based on additive tangent MoriâĂŞTanaka scheme. *Composites Part B: Engineering* 2019; 174.

46. Chaboche J, Kanouté P, Roos A. On the capabilities of mean-field approaches for the description of plasticity in metal matrix composites. *Int. Jounal of Plas.* 2005; 21: 1409-1434.

47. Wu L, Noels L, Adam L, Doghri I. An implicit-gradient-enhanced incremental-secant mean-field homogenization scheme for elasto-plastic composites with damage. *Int. Journal of Solids and Struc.* 2013; 50: 3843-3860.

48. Wu L, Noels L, Adam L, Doghri I. A combined incremental-secant mean-field homogenization scheme with per-phase residual strains for elasto-plastic composites. *Int. Journal of Plast.* 2013; 51: 80-102.

49. Wu L, Adam L, Doghri I, Noels L. An incremental-secant mean-field homogenization method with second statistical moments for elasto-visco-plastic composite materials. *Mechanics of Materials* 2017; 114: 180-200.

50. Haddad M, Doghri I, Pierard O. Viscoelastic-viscoplastic polymer composites: development and evaluation of two very dissimilar mean-field homogenization models. *Int. Journal of Sol. and Struct.* 2022.

51. Pierard O, Llorca J, Segurado J, Doghri I. Micromechanics of particle-reinforced elasto-viscoplastic composites: Finite element simulations versus affine homogenization. *Int. Journal of Plast.* 2007; 23: 1041-1060.

52. De Borst R, Sluys L, MÃijhlhaus H, Pamin J. Fundamental issues in finite element analyses of localization of deformation. *Eng. Comput.* 1993; 10: 99-121.

53. Bažant Z, Belytchko T, Chang T. Continuum theory for strain-softening. *Journal. Eng. Mech.* 1984; 110: 1666-1692.

54. Zbib H, Aifantis E. A gradient-dependent flow theory of plasticity: Application to metal and soil instabilities. *Appl. Mech. Rev.-T* 1989; 42: S295-S304.

55. De Borst R. Simulation of strain localization: a reapprisal of the Cosserat continuum. *Eng. Comput.* 1991; 8: 317-332.

56. Peerlings R, De Brost R, Brekelmans W, Ayyapureddi S. Gradient-enhanced damage for quasi-brittle materials. *Int. Journal Numer. Meth. Eng.* 1996; 39: 3391-3403.

57. Geers M. Experimental analysis and computational modelling of damage and fracture. *Ph.D. thesis. University of Technology, Eindhoven (Netherlands)* 1997.

58. Peerlings R, De Brost R, Brekelmans W, Geers M. Gradient-enhanced damage modelling of concrete fracture. *Mech. Cohes.-Frict. Mater.* 1998; 3: 323-342.

59. Aifantis E. On the role of gradients in the localization of deformation and fracture. *Int. Journal Eng. Sci.* 1992; 30: 1279-1299.

60. Svedberg T, Runesson K. A thermodynamically consistent theory of gradient-regularized plasticity coupled to damage. *Int. Journal Plast.* 1997; 13: 669-696.

61. Knockaert R, Doghri I. Nonlocal consitutive models with gradients of internal variables derived from a micro/macro homogenization procedure. *Comput. Meth. Appl. Mech. Eng.* 1999; 174: 121-136.

62. Liu X, Hu G. A continuum micromechanical theory of overall plasticity for particulate composites including particle size effect. *Int. Journal Plast.* 2005; 21: 777-799.

63. Coenen E, Kouznetsova V, Geers M. Enabling microstructure-based damage and localization analyses and upscaling. *Model. Simul. Mater. Sci. Eng.* 2011a; 19: 1-15.

64. Coenen E, Kouznetsova V, Geers M. Novel boundary conditions for strain localization analyses in microstructural volume elements. *Int. Journal Numer. Meth. Eng.* 2011b; 90: 1-21.

65. Massart T, Peerlings R, Geers M. A dissipation-based control method for the multi-scale modelling of quasi-brittle materials. *C.R. Méca.* 2005; 333: 521-527.

66. Massart T, Peerlings R, Geers M. An enhanced multi-scale approach for masonry wall computations. *Int. Journal Numer. Meth. Eng.* 2007; 69: 1022-1059.

67. Wu L, Noels L, Adam L, Doghri I. A multiscale mean-field homogenization method for fiber-reinforced composites with gradient-enhanced damage models. *Comp. Meth. in Appl. Mech. and Eng.* 2012; 233-236: 164-179.

68. Nguyen VD, Lani F, Pardoen T, Morelle XP, Noels L. A large strain hyperelastic viscoelastic-viscoplastic-damage constitutive model based on a multi-mechanism non-local damage continuum for amorphous glassy polymers. *International Journal of Solids and Structures* 2016; 96: 192-216.

69. Nguyen VD, Wu L, Noels L. A micro-mechanical model of reinforced polymer failure with length scale effects and predictive capabilities. Validation on carbon fiber reinforced high-crosslinked RTM6 epoxy resin. *Mech. of Mat.* 2019; 133: 193-213.

70. Melro A, Camanho P, Andrade Pires FM, Pinho S. Micromechanical analysis of polymer composites reinforced by unidirectional fibres: Part I – Constitutive modelling. *International Journal of Solids and Structures* 2013; 50: 1897-1905.

71. Chevalier J, Camanho P, Pardoen T. Multi-scale characterization and modelling of the transverse compression response of unidirectional carbon fiber reinforced epoxy. *Comp. Struct.* 2019.

72. Guéry AAC, Cormery F, Shao J, Kondo D. A micromechanical model of elastoplastic and damage behavior of a cohesive geomaterial. *International Journal of Solids and Structures* 2008; 45: 1406-1429.

73. Shen W, Shao J, Kondo D, Gatmiri B. A micro-macro model for clayey rocks with a plastic compressible porous matrix. *International Journal of Plasticity* 2012; 36: 64-85.

74. Kaiser J, Stommel M. Modified mean-field formulations for the improved simulation of short fiber reinforced thermoplastics. *Composites Science and Technology* 2014; 99: 75-81.

75. Kolling S, Haufe A, Feucht M, Bois PD. SAMP-1: a semi-analytical model for the simulation of polymers. *4. LS-DYNA Anwenderforum, Bamberg* 2005.

76. Doghri I, Brassart L, Adam L, Gerard J. A second-moment incremental formulation for the mean-field homogenization of elasto-plastic composites.. *International Journal of Plasticity* 2011; 27: 352-371.

77. Bornert M, Bretheau T, Gilormini P. Homogénéisation des milieux aléatoires : bornes et estimations.. *Homogénéisation en mécanique des matériaux* 2001; 1: 133-222.

78. Krairi A. Multiscale modeling of the damage and failure of homogeneous and short-fiber reinforced thermoplastics under monotonic and fatigue loadings. *Ph.D. Thesis* 2015.

79. Wu L, Zhang T, Maillard E, Adam L, Martiny P, Noels L. Per-phase spatial correlated damage models of UD fibre reinforced composites using mean-field homogenisation; applications to notched laminate failure and yarn failure. *Computers and Structures* 2021-12; 257. doi: 10.1016/j.compstruc.2021.106650

80. Al-Rub RA, Tehrani A, Darabi M. Application of a large deformation nonlinear-viscoelastic viscoplastic viscodamage constitutive model to polymers and their composites. *International Journal of Damage Mechanics* 2015; 24: 198-244.

81. Vogler M, Rolfed R, Camanho P. Modeling the inelastic deformation and fracture of polymer composites âĂŞ Part I: Plasticity model. *Mechanics of Materials* 2013; 59: 50-64.

82. Wu L, Ngunyen V, Noels L. An inverse micro-mechanical analysis toward the stochastic homogenization of nonlinear random composites. *Comp. Meth. in Appl. Mech. and Eng.* 2019; 348: 97-138.

83. E. Béchet eVN, Geuzaine C, Noels L. Imposing periodic boundary condition on arbitrary meshes by polynomial interpolation. *Comp. Mat. Sci.* 2012.

84. Verhoosel CV, Remmers JJC, GutiÃľrrez MA, Borst dR. Computational homogenization for adhesive and cohesive failure in quasi-brittle solids. *International Journal for Numerical Methods in Engineering* 2010; 83(8-9): 1155-1179. doi: https://doi.org/10.1002/nme.2854

85. Wu L, Chung CN, Major Z, Adam L, Noels L. From SEM images to elastic responses: A stochastic multiscale analysis of UD fiber reinforced composites. *Composite Structures* 2018; 189: 206 - 227. doi: https://doi.org/10.1016/j.compstruct.2018.01.051